Metal–Organic Frameworks for Water Harvesting from Air

Markus J. Kalmutzki,* Christian S. Diercks, and Omar M. Yaghi*

Dedicated to Susumu Kitagawa for his scholarship and friendship

Water harvesting from air in passive, adsorption-based devices holds great potential for delivering drinking water to arid regions of the world. This technology requires adsorbents that can be tailored for a maximum working capacity, temperature response, and the relative pressure range in which reversible adsorption occurs. In this respect, metal–organic frameworks (MOFs) are promising, owing to their structural diversity and the precision of their functionalization for adjusting both pore size and hydrophilicity, thereby facilitating the rational design of their water-sorption characteristics. Here, chemical and structural factors crucial for the design of hydrolytically stable MOFs for water adsorption are discussed. Prevalent water adsorption mechanisms in micro- and mesoporous MOFs alongside strategies for fine-tuning of their adsorption behavior by means of reticular chemistry are presented. Finally, an approach for the selection of promising MOFs with respect to water harvesting from air is proposed and design concepts for next-generation MOFs for application in passive adsorption-based water-harvesting devices are outlined.

1. Introduction

Water is the single most indispensable natural resource for life on earth as best described by Leonardo Da Vinci's conclusion that "water is the driving force of all nature" (vetturale di natura).[1] Today, providing fresh water to a rapidly growing world population is a great societal challenge. Of all water on earth only 2.5% is fresh water—the main part being locked up in glaciers (68.7%), stored in groundwater (30.1%), and only a small fraction being directly accessible in rivers and lakes (0.4%).[2] With two thirds of the world's population experiencing water stress, it is unlikely that these sources of fresh water will suffice to address this challenge.[3] The main fraction of water, 96.5%, is contained within the oceans thus precluding direct utilization as

drinking water. While technically feasible, desalination of sea water requires energy intensive processes to produce water of drinking water quality.[4] More importantly, many of the countries experiencing water stress are landlocked, further highlighting the need for alternative ways of accessing drinking water. One alternative resource that can be accessed is the humidity in the earth's atmosphere. It holds water in the form of vapor and droplets (humidity), adding up to about 10% of all other fresh-water resources. This equals an estimated 13 000 trillion liters of water available in the atmosphere at any one time that could be used to address the global water problem. There have been efforts to collect water from fog and moist air and two general concepts, fog collectors and adsorption based systems, have been proposed.[5] Fog collectors require permanent high relative humidity (RH ≈ 100%) levels and light winds to facilitate dewing on fine nets, and this severely restricts the geographical areas suitable for their application. In contrast, the concept of adsorption based devices has a high potential for water harvesting, even from dry air, but is strongly dependent on the performance of the adsorbent. As of now, the water uptake of classical desiccants (e.g., $CaCl_2$, silica gel, or zeolites) employed in such devices is high but their strong affinity to water renders their regeneration energy intensive, thereby leading to low working capacities in autonomous devices, especially when powered by low grade energy sources.[6] Therefore, the development of novel adsorbents is needed in order to propel adsorption based water harvesting devices from scientific curiosities into real-life applications. Next generation adsorbents should have: (i) high chemical stability to water, (ii) tailorable hydrophilicity, and (iii) an adjustable pore diameter to fine-tune the adsorption profile and modulate the sorption kinetics. Metal–organic frameworks (MOFs) hold promise to meet all of the aforementioned requirements as their modular construction from molecular building blocks and the large diversity of the resulting structures allow for the chemical and geometrical optimization necessary to achieve the desired water sorption properties.

While the adsorption of gases such as H_2, CH_4, and CO_2 has been extensively studied and principles regarding the design of MOFs displaying high uptake of these gases have been established, water sorption has received significantly less attention. This may be due to the fact that the first generation of MOFs often showed low stability in the presence of water. Today, however, this issue has been resolved and many MOFs with high

Dr. M. J. Kalmutzki, C. S. Diercks, Prof. O. M. Yaghi
Department of Chemistry
Kavli Energy NanoScience Institute
and Berkeley Global Science Institute
University of California – Berkeley
Berkeley, CA 94720, USA
E-mail: mjkalmutzki@berkeley.edu; yaghi@berkeley.edu
Dr. M. J. Kalmutzki, C. S. Diercks, Prof. O. M. Yaghi
Materials Sciences Division
Lawrence Berkeley National Laboratory
Berkeley, CA 94720, USA
Prof. O. M. Yaghi
King Abdulaziz City for Science and Technology (KACST)
P.O. Box 6086, Riyadh 11442, Saudi Arabia

water-stability have been reported. With respect to real-life applications as well as to the development of next-generation MOFs for water harvesting, a thorough understanding of the degradation mechanisms in the presence of water is necessary. In Section 1 of this review we will focus on the hydrolytic stability of MOFs and discuss prevalent degradation mechanisms. In addition to a high water-stability, for a MOF to be suitable for water harvesting from air it needs to show a high reversible water uptake between 10% and 30% relative humidity (RH), the region that defines the deliverable capacity in passive water harvesting devices. For a material to operate efficiently in this region water needs to interact relatively strongly with the adsorbent, but at the same time the strength of this interaction should be weak enough to allow for temperature swing adsorption (TSA) using low-grade, renewable energy sources (e.g., solar–thermal heating, waste heat, geothermal energy) or pressure swing adsorption (PSA) within the limits of a typical day-night cycle.[7] The water adsorption properties, i.e., the slope of the isotherm and its inflection point on the P/P_0 scale are mainly governed by the pore size, the hydrophilicity, and the chemical nature of the adsorbent. Section 2 deals with different adsorption mechanisms, while Section 3 will focus on single component water adsorption isotherms and their optimization by means of reticular chemistry. Section 4 will illustrate the working principles of water harvesting devices based on MOFs, highlight promising materials and provide guidelines for the proper selection and the design of next generation materials for water harvesting from air.

Markus J. Kalmutzki earned his diploma from the University of Tuebingen in 2010, where he also received his Ph.D. in 2014. From 2014 to 2015, he worked with Prof. H.-Juergen Meyer as a postdoctoral fellow. He is currently a DFG fellow in the group of Prof. Omar M. Yaghi, at the University of California, Berkeley, where his research is focused on the synthesis and characterization of new MOFs and the study of their physical properties.

Omar M. Yaghi received his Ph.D. from the University of Illinois-Urbana (1990), and studied as a postdoctoral fellow at Harvard University. He is currently the James and Neeltje Tretter Professor of Chemistry, University of California, Berkeley, and Senior Faculty Scientist at Lawrence Berkeley National Laboratory. His research encompasses stitching together organic and inorganic molecules by strong bonds to make crystalline extended porous structures, such as MOFs, ZIFs, and COFs. This field is referred to as reticular chemistry.

2. Stability of MOFs in the Presence of Water

A prerequisite for using MOFs in water harvesting applications is their hydrolytic stability. An understanding of degradation mechanisms and the principles for the design of MOFs with appropriate water stability are required in order to devise next generation water adsorbents.

2.1. Experimental Methods Used to Characterize Water Stability

In addition to computational methods, several analytical techniques are frequently used to gain insight into the degradation of MOFs in the presence of water. Since there are no standardized procedures defining the relative humidity, soaking time, or temperature during the stability assessment, the comparability between different studies is generally not given.[8] This can be ascribed to the fact that MOFs are implemented into many different applications that require different levels of hydrolytic stability. Therefore, it is important to select conditions mimicking those, the material will be exposed to in the envisioned application. In order to understand the isolated effect of water vapor on the structure, inert carrier gases such as N_2, He, or Ar should be chosen, true water adsorption isotherms however can only be recorded by dosing water vapor in the absence of a carrier gas. Minimum testing conditions for MOFs used in "single-pass" and "cycled" water sorption applications, as well as liquid phase separation have been established, and are given in **Table 1**.[9]

Analytical methods used to determine the stability of MOFs that provide insight into their degradation mechanisms can be classified into ex situ and in situ methods. The degradation of MOFs in the presence of water is often accompanied by a (partial) loss of crystallinity, which is why the comparison of X-ray diffraction patterns collected before and after exposure to humidity is often used to assess their stability. In situ diffraction experiments under different conditions (i.e., partial pressures of water, temperatures) can help to pinpoint changes in the crystal structure, allowing for the determination of degradation mechanisms.[10] Unstable compounds typically show a broadening of the reflections or even complete amorphization upon exposure to moisture, thus giving qualitative information on the stability as illustrated recently for two isostructural compounds, $Mn_2Cl_2(BTDD)$ and $Co_2Cl_2(BTDD)$ [where BTDD is bis(1H-1,2,3-triazolo[4,5-b],[4′,5′-i])dibenzo[1,4]dioxin].[11] Whereas the powder X-ray diffraction (PXRD) pattern of $Co_2Cl_2(BTDD)$ showed no significant changes after exposure to water vapor, that of $Mn_2Cl_2(BTDD)$ indicated amorphization of the MOF. It should be noted that even though $Co_2Cl_2(BTDD)$ showed no sign of structural degradation in PXRD studies, a decrease of the capacity of about 6% was observed after 30 subsequent hydration and dehydration cycles. Therefore, the substantiation of PXRD data with multiple water adsorption cycles is

**ADVANCED
SCIENCE NEWS**
www.advancedsciencenews.com

**ADVANCED
MATERIALS**
www.advmat.de

Table 1. Testing conditions for the assessment of the hydrolytic stability of MOFs for different types of application and appropriate analytical methods are proposed.

Application	Recommended testing conditions	Recommended characterization methods
Gas or vapor phase		
Single pass/one-time use		
• Single pass cartridge (e.g. gas mask or air filters)	Prolonged stability in ambient or humidified air	PXRD[a] and sorption (BET)[b] measurements
Cycled/multiple use		
• Gas separation: packed bed (e.g., CO_2, NG, H_2)	Multiple adsorption desorption cycles with the relevant gas mixture (regeneration using the appropriate method; TSA, PSA, VSA)[c]	PXRD, sorption (BET) measurements, adsorption capacity for each cycle, microscopy (e.g., SEM[d], TEM[e])
• Gas separation: membranes	Prolonged exposure to the relevant gas mixture under application conditions	PXRD, sorption (BET) measurements, microscopy (e.g., SEM, TEM, AFM[f])
• Gas storage (e.g., H_2, CH_4, CO_2)	Prolonged storage of the relevant gas under application pressures	PXRD and sorption (BET) measurements, microscopy (e.g., SEM, TEM)
• Water harvesting	Multiple adsorption desorption cycles under the relevant application conditions (humidity, temperature), immersion and prolonged stirring	PXRD, gas sorption (BET) measurements, determination of the inflection point and the water adsorption capacity for each cycle, microscopy (e.g., SEM, TEM), solid state mass loss, titration of the solution
Aqueous phase		
Liquid phase catalysis, liquid phase separation	Immersion and prolonged stirring under relevant application conditions	PXRD and sorption (BET) measurements, solid state mass loss, titration of the solution

[a]Powder X-ray diffraction; [b]Brunauer–Emmet–Teller surface area; [c]Temperature, pressure, vacuum swing adsorption; [d]Scanning electron microscopy; [e]Transmission electron microscopy; [f]Atomic force microscopy.

recommended. Degradation can also occur by partial dissolution of the material. This pathway inevitably leads to a mass loss and can be quantified by weighing of the material before and after water exposure. The formation of a minor amorphous side phase or dissolution of the material can however not be detected using crystallographic techniques. PXRD measurements are therefore generally substantiated with gas adsorption data collected before and after exposure to humidity and a comparison of the surface areas calculated from these measurements.

Changes of the material on the macroscopic scale, such as the formation of cracks or surface degradation can give valuable information on the degradation pathway. Scanning electron microscopy (SEM) studies showed that the degradation of HKUST-1 [$Cu_3(BTC)_2(H_2O)_3$, where BTC = benzene tricarboxylate] crystals is highly dependent on the temperature. Degradation of the crystal surface was observed after 3 d at 40 °C (90% RH), while at 25 °C the bulk of the crystal degraded faster than the surface.[12]

In situ infrared spectroscopy (IR) has been used to determine the water reaction pathway in (M)MOF-74 [$M_2(DOT)$ where M = Mg, Co, Zn and DOT = 2,5-dihydroxy-therephthalate]. It was shown that while water adsorption at room temperature below the condensation pressure is reversible, at elevated temperatures (150 °C) a reaction takes place even at low water vapor pressures.[13] Increased intensity of the carboxylic acid vibrational bands in the IR spectrum of HKUST-1 after 6 months at ambient conditions revealed that the degradation takes place by hydrolysis of the metal-linker bond.[14] Recently the degradation of cubic MOFs built from $Zn_4O(COO_2)_6$ secondary building units (SBUs) has been studied by positronium annihilation lifetime spectroscopy, an in situ method allowing for the time-resolved study of the porosity evolution.[15] It was shown

that the induction phase of the degradation strongly depends on previous water exposure of the MOF (history dependence). Lastly, the sensitivity of nuclear magnetic resonance (NMR) spectroscopy toward minor perturbations in the local structure (short-range order) make it an important tool in elucidating structural changes that cannot be detected using methods providing averaged structural information. Several probes have been used in solid-state magic angle spinning (MAS) NMR experiments to monitor structural changes in MOFs, however mostly not related to the structural degradation in the presence of water.[16] In MOFs constructed from deuterated linkers flipping rates of aryl units have been determined using ^{2}H-NMR.[17] ^{1}H- and ^{13}C-NMR have been proven useful in tracking structural changes in HKUST-1 at different water loadings indicating different degradation pathways at different RH values.[18] Many metals frequently used to construct the SBUs of MOFs have isotopes that are NMR active (e.g., ^{27}Al, ^{57}Fe, ^{63}Cu, ^{71}Ga, ^{89}Y, ^{115}In) allowing the measurement of changes in the local environment of the SBU upon exposure to water. While the above-mentioned methods give information about the stability of materials, they provide little to no direct information on the mechanisms of degradation.

2.2. Degradation Mechanisms of MOFs in the Presence of Water

The two pathways for the degradation of MOFs in the presence of water are hydrolysis and linker displacement. Both have been established for MOFs built from $Zn_4O(COO)_6$ SBUs by calculations and confirmed experimentally.[19] Hydrolysis occurs when the metal-linker bond is broken by addition of

hydroxyl groups resulting in the liberation of a free, protonated linker (Equation (1)), while the linker displacement mechanism involves insertion of water into the metal-linker bond, followed by the release of a free, deprotonated linker (Equation (2))
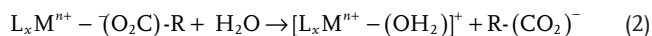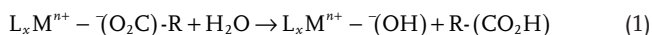
$$L_x M^{n+} - {}^-(O_2C)\text{-}R + H_2O \rightarrow L_x M^{n+} - {}^-(OH) + R\text{-}(CO_2H) \qquad (1)$$

$$L_x M^{n+} - {}^-(O_2C)\text{-}R + H_2O \rightarrow [L_x M^{n+} - (OH_2)]^+ + R\text{-}(CO_2)^- \qquad (2)$$

Figure 1 illustrates the degradation of UiO-66 [$Zr_6O_4(OH)_4(BDC)_6$, where BDC = 1,4-benzenedicarboxylate] following a linker displacement mechanism in the presence of water or base and a substitution mechanism similar to that of hydrolysis in the presence of acids.[20] Treatment with alcohols such as methanol follows a mechanism similar to that shown for water. It was suggested that clustering of water molecules around the SBU drives the degradation of MOFs.[21] Theoretical studies of the degradation mechanisms of hydrophobic MOFs built from basic zinc carboxylate SBUs revealed that water does not only play an important role in replacing the linker but that additional water molecules stabilize, by solvation, the hydrolyzed SBU as well as the expelled linker.[22] The stability of MOFs is influenced by thermodynamic and kinetic factors and their precise adjustment is crucial for the development of next generation materials with appropriate hydrolytic stability.
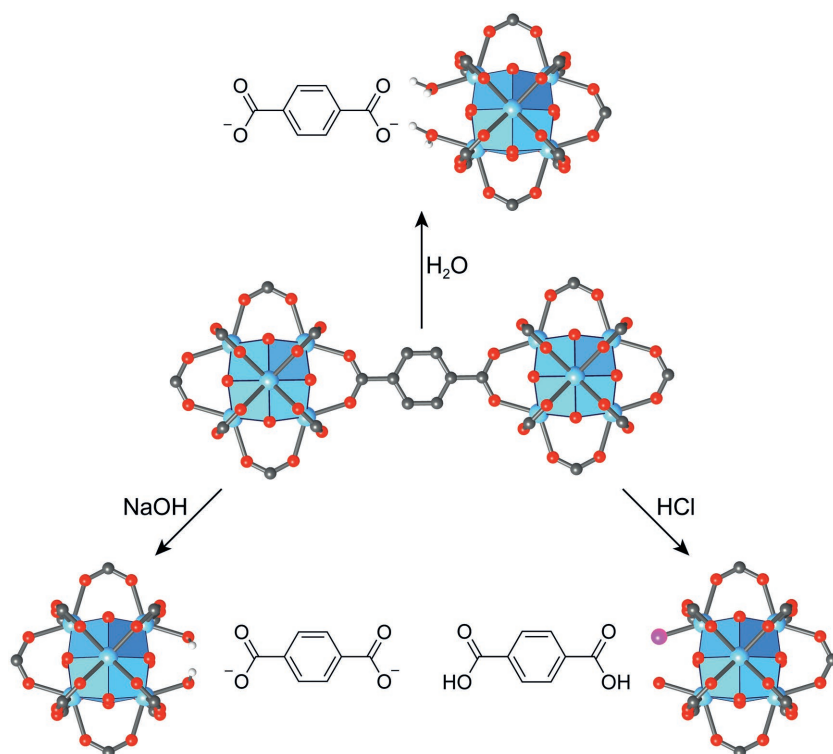
2.3. Thermodynamic Parameters Influencing the Hydrolytic Stability of MOFs

The two factors determining the thermodynamic stability of MOFs are the strength of the metal-linker bond, and the energetic positioning of the frontier orbitals on the metal ions with respect to those of water. The linkers and the SBU are both chemically stable entities, hence the bond between them can be considered the weak point of extended structures, formed by their reticulation. It was shown that within certain limitations the strength of the metal-linker bond can constitute a direct indicator of the hydrolytic stability.[19] This is however not generally the case. The binding groups of the organic linker and the metal centers of the SBU can be regarded as Lewis acid–base pairs. The strength of their interaction is therefore governed by the basicity of the deprotonated linker and the acidity of the metal ion. This principle was first discussed in the context of pyrazolate based MOFs which display high chemical stability.[23] A comparison of linkers bearing pyrazolate and carboxylate groups arranged around a central aryl unit reveals dramatic differences in pK_a between the two binding groups (see **Figure 2**a). The pK_a is an especially useful tool in the design of thermodynamically stable MOFs, since values of organic molecules are readily available in tables or can be calculated using commercially available software.[24] pK_a values of the metal centers can be approximated based on their charge and radius. Highly charged metals such as Ti^{+4}, Zr^{+4}, and Hf^{+4} tend to form MOFs with high stability toward water as illustrated by frameworks such as UiO-66 [$Zr_6O_4(OH)_4(BDC)_6$], MOF-801 [$Zr_6O_4(OH)_4(fumarate)_6$], or DUT-67 [$Zr_6O_6(OH)_2(TDC)_4(Ac)_2$, where TDC = 2,5-thiophenedicarboxylate and Ac = acetate].[7,25] Recently it was reported, that highly charged U^{+6} can be used to prepare an ionic framework with outstanding water-stability.[26] More precise considerations should also include the polarizability of the metal. A simplified way for matching the metal used to construct the SBUs to the binding groups connecting them is the hard-soft acid–base concept. This concept states that strong bonds are formed by overlapping frontier orbitals of similar size and polarizability. Since binding groups with a high pK_a values—generally hard bases—provide for strong bonding, stable MOFs based on carboxylate, pyrazolate, or tetrazolate linkers are mainly formed from metals that can be described as hard acids (see Figure 2b).

The susceptibility of different metals to be attacked by water molecules heavily depends on the energetic positioning of their frontier orbitals with respect to those of water. As a rule of thumb, for a series of isoreticular MOFs constructed from different metals, those MOFs containing metals with lower reduction potentials (i.e., E_0 is lower or has a more negative value) are more likely to be attacked by water and are hence less hydrolytically stable.[27] Comparison of the water stability of the
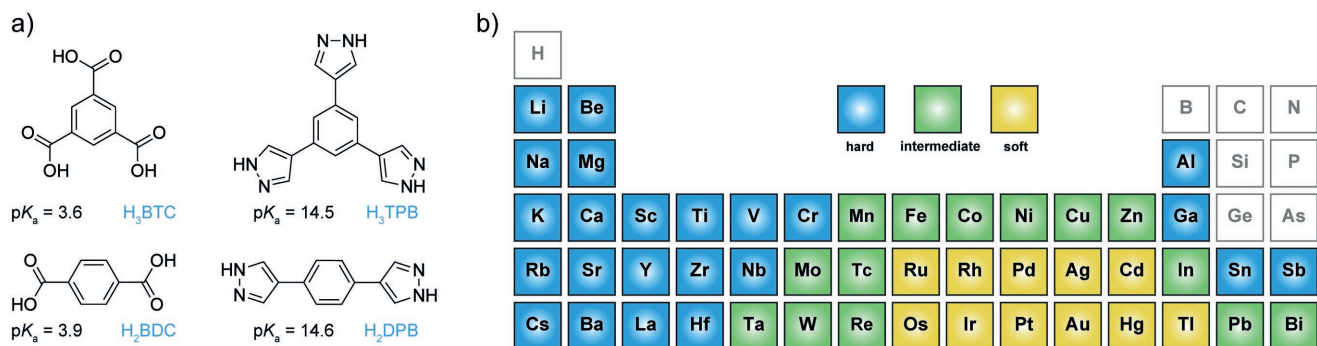

Figure 1. Degradation of the structure of UiO-66 following a linker displacement mechanism in the presence of water (top) or base (left). In the presence of hydrochloric acid, a substitution mechanism similar to that of hydrolysis is observed.[20] The structures of the degradation products are modeled based on the original crystal structure of UiO-66.

ADVANCED
SCIENCE NEWS
www.advancedsciencenews.com

ADVANCED
MATERIALS
www.advmat.de

Figure 2. a) Comparison of the pK_a values of a) carboxylic acid and pyrazole linkers. b) The classification of metals within the periodic table into soft (yellow), intermediate soft/hard (green), and hard acids (blue).

two isostructural compounds $Co_2Cl_2(BTDD)$ ($E_0 = -0.28$ eV) and $Mn_2Cl_2(BTDD)$ ($E_0 = -2.37$ eV) shows that the former is more stable toward water than the latter, which was in fact shown to undergo hydrolysis as indicated by amorphization of the sample. This finding is in good agreement with the stability expected based on the reduction potentials of the two metals.[11]

2.4. Kinetic Parameters Influencing the Hydrolytic stability of MOFs

While the thermodynamic stability is related to the free Gibbs energy (ΔG) of the degradation reaction, the kinetic inertness is related to its activation energy (E_a) as illustrated in **Figure 3**. A thermodynamically unstable MOF can therefore be stable in the presence of water due to kinetic reasons. There are multiple structural factors that render MOFs kinetically inert; (i) steric
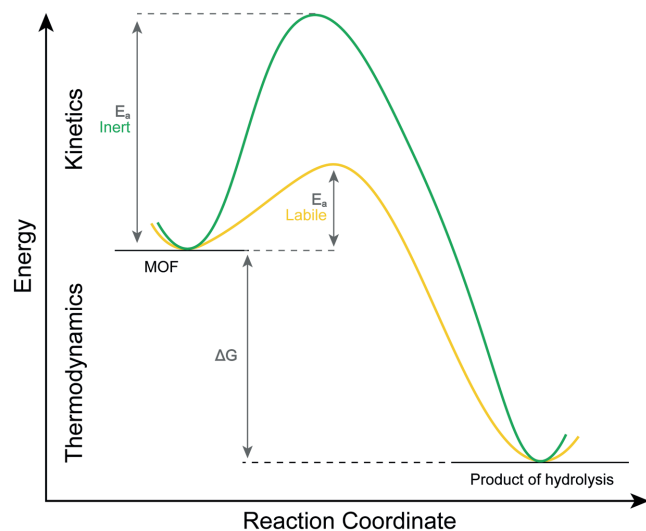

Figure 3. Reaction coordinate diagram illustrating the hydrolysis of MOFs. The thermodynamic stability is defined by the Gibbs' free energy (ΔG). Kinetic inertness is defined by the activation energy (E_a) required to reach the transition state. The green graph represents a kinetically inert MOF with a high E_a for the hydrolysis reaction, whereas the yellow line represents a kinetically labile MOF, where little energy is needed to reach the product-like transition state. Both materials are thermodynamically unstable.

hindrance and rigidity of the SBU and/or the linker, (ii) steric hindrance through interpenetration, (iii) the electronic configuration of the metal, and (iv) hydrophobicity.

2.4.1. The Rigidity of the Building Blocks and Steric Shielding

The degradation of MOFs relies on water molecules being able to approach the SBUs and form water cluster in their vicinity.[21] Steric shielding can inhibit or slow down the diffusion of water to the metal centers of the SBU. Three different ways to introduce steric shielding in MOF structures, resulting in an increased water stability have been reported; (i) SBUs with high connectivity, (ii) bulky linkers, and (iii) catenation. It was also shown that frameworks built from rigid building blocks are less likely to undergo degradation by linker displacement.

Bulky binding groups and substituents appended to the linker can effectively shield the metal centers in the SBUs from water. Shielding of the SBU by the binding groups of the linker is more efficient, the higher the connectivity of the SBU. Highly connected nets are often observed in MOFs built from highly charged metals such as zirconium and hafnium. A prominent example of a zirconium based MOF with high connectivity is UiO-66, built from 12-connected $Zr_6O_4(OH)_4$ SBUs stitched together by ditopic BDC linkers, forming a framework of **fcu** topology (Figure 11).[25a] The high connectivity provides for steric shielding of the SBU and UiO-66 indeed shows high stability toward water.[12,28] Other MOFs built from 12-connected SBUs sharing the same $M_6^{4+}(OH)_4O_4$ core also show similar hydrolytic stability.[29] In all of these cases, steric shielding is not exclusively due to the binding groups of the linker but the bulkiness of the linker itself and the pore size also play pivotal roles. The isoreticular expanded version of UiO-66 (UiO-67 [$Zr_6O_4(OH)_4(BPDC)_6$] where BPDC = biphenyl-4,4′-dicarboxylate) displays a significantly lower stability toward water than the parent isoreticular UiO-66. The original stability can be restored by virtue of appending large substituents to the BPDC linker to effectively increase steric shielding, an effect that will be discussed later in more detail.[30] MOFs built from infinite, rod-like SBUs are often exceptionally stable because of steric shielding by the binding groups. **Figure 4** gives selected examples of SBUs with high connectivity found in MOFs with outstanding water stability. The space filling representation highlights the steric shielding of the
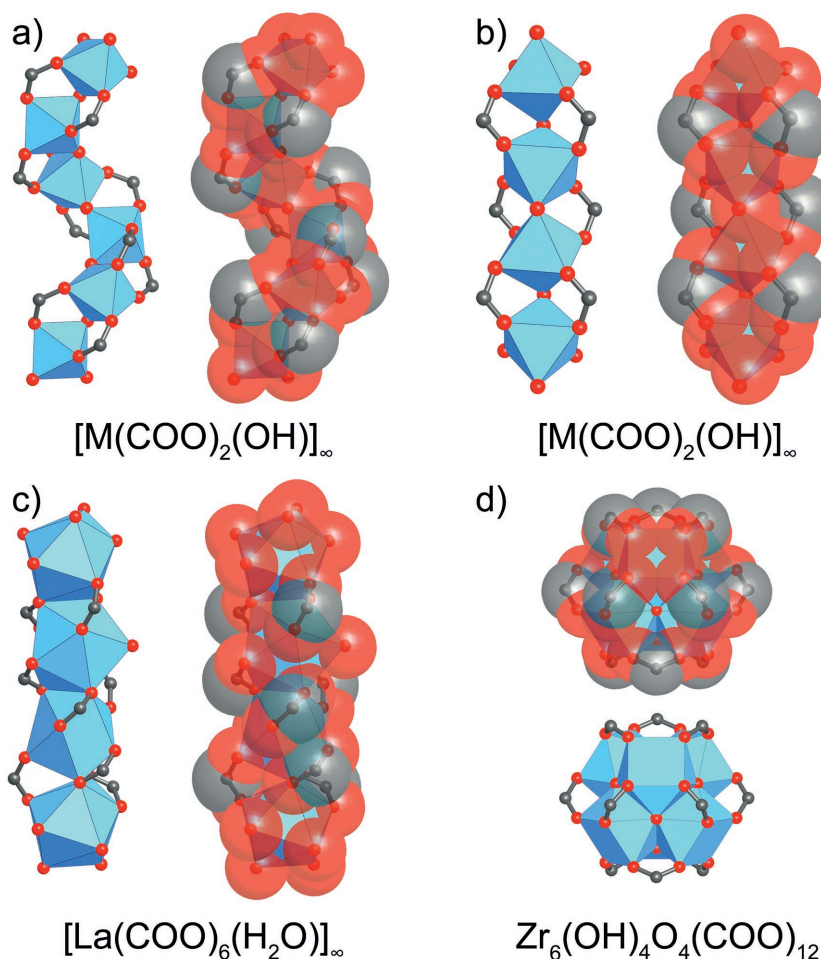
**ADVANCED
SCIENCE NEWS**

www.advancedsciencenews.com

**ADVANCED
MATERIALS**

www.advmat.de

Figure 4. Selection of SBUs with high connectivity found in MOFs that display high stability in the presence of water: a) CAU-10, b) MIL-53, c) La(BTB)$_3$, and d) UiO-66. The SBUs are represented as polyhedra both with and without space filling R-COO$^-$ binding groups to highlight the kinetic inertness of the SBUs due to steric shielding.

built from 2D Zn(BDC)-layers of **sql** topology, pillared by DABCO to form a 3D network structure with an overall **pcu** topology, was shown to allow for the precise adjustment of its water stability.[34] In the presence of water the zinc paddle wheel SBUs in the parent MOF readily hydrolyze, leading to structural degradation. Increased steric shielding by virtue of appended methyl groups on the H$_2$BDC linker allows for the systematic tuning of the kinetic water stability of DMOF derivatives.[35] The increase in stability cannot be rationalized by the more hydrophobic nature of alkyl substituted DMOF derivatives alone.[35] A comparison of the inflection points allowing for the assessment of the relative hydrophilicities is however not possible since pristine DMOF degrades in the presence of water. The shielding effect of (CH$_3$)$_2$-BDC and (CH$_3$)$_4$-BDC in the structure of DMOF is illustrated in **Figure 5**. A similar, yet less pronounced effect has been observed for a series of isoreticular MOFs (IRMOFs) where the BDC linker was replaced by (Me)$_2$BDC and 2-(CF$_3$O)BDC.[36] Both IRMOFs showed an increased stability toward water compared to the parent MOF-5. The shielding effect in these examples is achieved by introducing hydrophobic functional groups which also inevitably leads to a lower water uptake compared to the parent MOF due to a decreased pore volume. Appended polar (hydrophilic) functional groups such as amines and alkoxy groups can also increase the stability of MOFs. These polar groups shield the SBU from water by acting as basins of attraction that draw water away from the SBU.[37] The stabilization due to catenation can also be rationalized by steric shielding, and it has been shown in several cases that the

SBU, which by virtue of its high connectivity has been proven to be a key feature in designing water stable MOFs.[7,25b,31]

Another approach to tuning the kinetic water stability of MOFs is to append bulky substituents to the organic linker.[32] This approach allows for the adjustment of the water stability by rational linker design. Studies regarding the impact of linker functionalization on the water stability of a series of quaternary MOFs based on MUF-7a revealed that linkers conferring a higher degree of rigidity may inhibit their displacement by water following a linker displacement mechanism, thereby endowing the framework with increased stability.[33] It should however be noted, that the more rigid linkers studied in this report are also more hydrophobic and the increased stability toward water can therefore not solely be attributed to their enhanced rigidity alone. The stronger hydrophobicity of the tritopic truxene-based linkers used to construct MUF-77 compared to the H$_3$BTB (1,3,5-tris(4-carboxyphenyl)benzene) linker employed in the synthesis of MUF-7a was evidenced by a shift of the inflection point to higher relative pressures (higher value of α) for all modified MOFs. The functionalization of the BDC linker in DMOF [Zn(BDC)(DABCO)$_{0.5}$, where DABCO = 1,4-diazabicyclo[2.2.2]octan], a MOF

water stability of interpenetrated frameworks is higher than that of their non-interpenetrated counterparts.[38] Catenation is necessarily accompanied by a decrease in pore-size and from a topological point of view it is not always possible to prepare an interpenetrated form of every MOF structure. Strategies relying on the introduction of additional functionalities or even additional interpenetrating frameworks into the pores inevitably lead to a decrease in the accessible pore volume and consequently to lower maximum capacities as compared to the parent MOFs. Therefore, in the context of water harvesting from air, the concept of increasing the hydrolytic stability by steric shielding based on bulky linkers or interpenetration of framework is less useful than other strategies, where an increase in stability does not result in a decrease of the pore volume.

2.4.2. The Electronic Configuration of the Metal Center

Kinetic inertness of the metal centers constituting the SBUs can increase the water stability of thermodynamically unstable compounds, a concept well-established in coordination chemistry. The electronic configuration of the metal centers of the
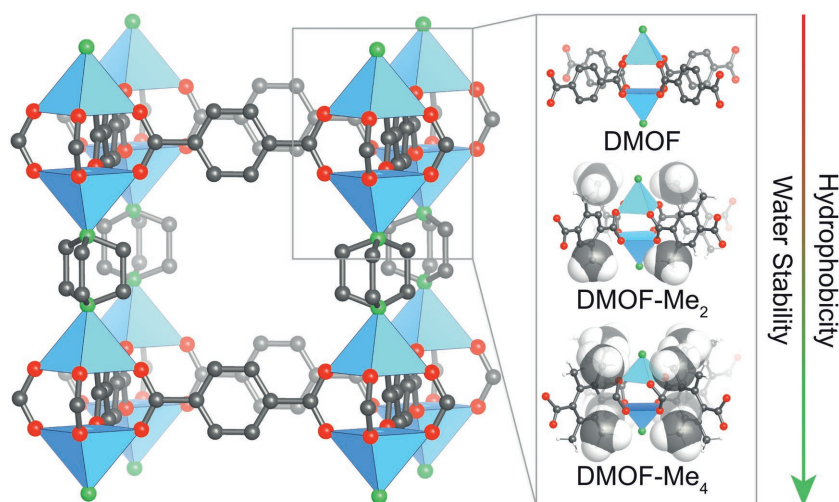
Figure 5. Increased water stability of DMOF by rational linker design. The steric shielding of the paddle wheel SBUs by additional methyl substituents on the BDC linker is illustrated. Both the water stability and hydrophobicity of the material increase by appending two or four methyl groups.[36]

SBUs can provide information about the kinetic inertness and thus the hydrolytic stability of MOFs. Both iron and chromium MIL-101 $[M_3O(H_2O)_2(L)(BDC)_3$ where L = OH or F] show outstanding water stability. It can be argued that this stability originates from the electronic configuration of the metal centers within the sterically unhindered $M_3O(COO)_6L_3$ SBUs.[39] (Cr) MIL-101 is stable enough to allow for the encapsulation of acidic moieties such as phosphotungstic acid (PTA) in aqueous reaction media.[40] A comparison of (M)MIL-53 [(M)(OH)BDC, where M = Al or Cr] and (V)MIL-47 [V(O)BDC], three MOFs of the same general structure (**sra** topology), revealed that the chemical stability of these MOFs follows the order $Cr^{+3} > Al^{+3} > V^{+4}$ which is in good agreement with the decreasing inertness $Cr^{+3} > Al^{+3} > V^{+3} > V^{+4}$. In contrast, the bond strength of the M−O bond (calculated for the corresponding oxides) follows the reverse order $V^{4+} > Al^{3+} > Cr^{3+}$.[41] Here, the kinetic inertness defines the stability toward water, whereas the strength of the metal-linker bond is correlated to the thermal stability of these MOFs. The large difference in energy between the frontier orbitals of Cr^{3+} and those of water also contributes to the outstanding water stability of (Cr)MIL-53.[9]

2.4.3. Hydrophobicity

The structural degradation by hydrolysis or linker displacement is initiated by the formation of water clusters close to the SBU prior to diffusion of water molecules to the metal centers. The formation of water clusters in close proximity to the SBUs can be avoided by decorating the linker with hydrophobic fluorinated functional groups or alkyl groups.[32b,36b,42] It was also shown that polar functional groups (e.g., amines, alkoxy groups) can have similar impact on the water stability of MOFs by drawing water away from the SBU, influencing the basicity of the linker, and/or influencing the mobility of water in the vicinity of the SBU.[37]

Depending on the chemical nature of the MOF, two types of hydrophobicity can be distinguished; internal and external. Internal hydrophobicity allows for water to enter the pore system but prevents it from getting too close to the SBU, whereas external hydrophobicity prevents water from entering the pore system and can be directly quantified by measuring the contact angle on the surface of the materials.[43] Different strategies have been employed in the synthesis of hydrophobic MOFs.

Partial fluorination was shown to endow MOFs based on copper paddle wheel SBUs with considerable water stability. Water adsorption isotherms of $Cu_2(L)(H_2O)_2$ (L = 2′-amino-5′-fluoro-(1,1′:3′,1″-terphenyl)-3,3″,5,5″-tetracarboxylic acid) show a maximum uptake of 0.32 g g^{-1} alongside a strong hysteresis. A steep uptake is recorded at high relative pressures (P/P_0 = 0.85, indicative of a hydrophobic pore system.[44] In situ IR spectroscopy and adsorption experiments, substantiated by first-principles density functional theory (DFT) calculations showed that the negligible water uptake in the hydrophobic pores in FMOF-1 $[Ag_2(Ag_4Tz_6)]$, where Tz = 3,5-bis(trifluoromethyl)(1,2,4-triazolate)] is due to the formation of pentameric water clusters in the large cavities of the structure.[42b] The inability of water to enter the pore system of such MOFs renders them unsuitable for water-adsorption-based applications, however, they are ideal candidates for applications in separation, such as the separation of C6–C8 hydrocarbons of oil components.[45] Another approach to introduce hydrophobicity is the successive addition of methyl groups to the organic backbone of the framework. This was illustrated for a MIL-53 analogue [Al(OH)(1,4-NDC), where 1,4-NDC = 1,4-naphthalenedicarboxylate] where decoration of the linker with methyl groups results in a shift of the inflection point of the isotherm to higher relative pressures and a decrease in the maximum water uptake, which is in good agreement with the increased hydrophobicity of the pores and the reduced pore volume due to the additional substituents appended to the linker.[46] Zeolitic imidazolate frameworks (ZIFs) are generally hydrophobic in nature. The hyperhydrophobicity of ZIF-8 results in a negligible water uptake, even at pressures near to the bulk saturation pressure.[21,47] Many other ZIFs such as ZIF-71, a ZIF built from dcIM (dcIM = 4,5-dichloroimidazolate) linkers show a similarly strong hydrophobicity. This can be attributed to the combination of the lack of polar centers and the small pore openings.[48] The hydrophobicity of ZIFs can be decreased by installation of polar functionalities in the 5-position of the imidazolate linkers. ZIF-90, a ZIF of **SOD** topology built from an aldehyde substituted imidazolate linker, shows a water uptake of 0.29 g g^{-1}, consistent with the free pore volume of this compound.[49] It is worthy of note, that increasing the water stability of MOFs by means of hydrophobicity limits their capability with respect to water adsorption, especially, water harvesting from air which requires water adsorption to occur at low relative pressures. Low inflection points are an indicator

**ADVANCED
SCIENCE NEWS**

www.advancedsciencenews.com

**ADVANCED
MATERIALS**

www.advmat.de

for a hydrophilic pore system and cannot be realized in hydrophobic materials.

3. Water Adsorption Mechanisms

Water adsorption in MOFs can occur following three distinct mechanisms: (i) chemisorption on open metal sites, (ii) physisorption in the form of layers or clusters, and (iii) capillary condensation.

3.1. Chemisorption on Open Metal Sites

In many MOF structures, the coordination sphere of the metal ions constituting the SBU is completed by neutral donor ligands as in the case of MOFs built from paddle wheel (e.g., HKUST-1) and many rod-like SBUs (e.g., MOF-74).[50] These neutral ligands can typically be removed by heating under vacuum. In contrast to HKUST-1, which, similar to other

copper paddle wheel based MOFs, displays low water stability, most compounds of the isoreticular (M)MOF-74 (M = Mg^{2+}, Zn^{2+}, Ni^{2+}, Co^{2+}) series display a comparatively high hydrolytic stability.[12,21] The crystal structure of (M)MOF-74 materials is built from helical, rod-like SBUs that are connected by linear DOT linkers to form frameworks of **etb** topology resembling a honeycomb structure with hexagonal 1D channels of ≈11 Å running along the crystallographic *c*-axis. In its solvated form, terminal water ligands on the SBUs pointing at the center of the pores, complete the coordination sphere of the metal centers. When fully activated, these terminal ligands are removed and leave behind open metal sites (see **Figure 6**a). DFT calculations on fully activated (Mg)MOF-74 show that a large unoccupied orbital is located on those open metal sites.[51] Single crystal X-ray diffraction studies on hydrated (Zn)MOF-74 revealed the presence of three distinct adsorption sites of various strength that can be distinguished based on their thermal ellipsoids (Figure 6b).[52] The strong bonding of water molecules chemisorbed on the open metal sites is reflected by small thermal ellipsoids whereas water molecules
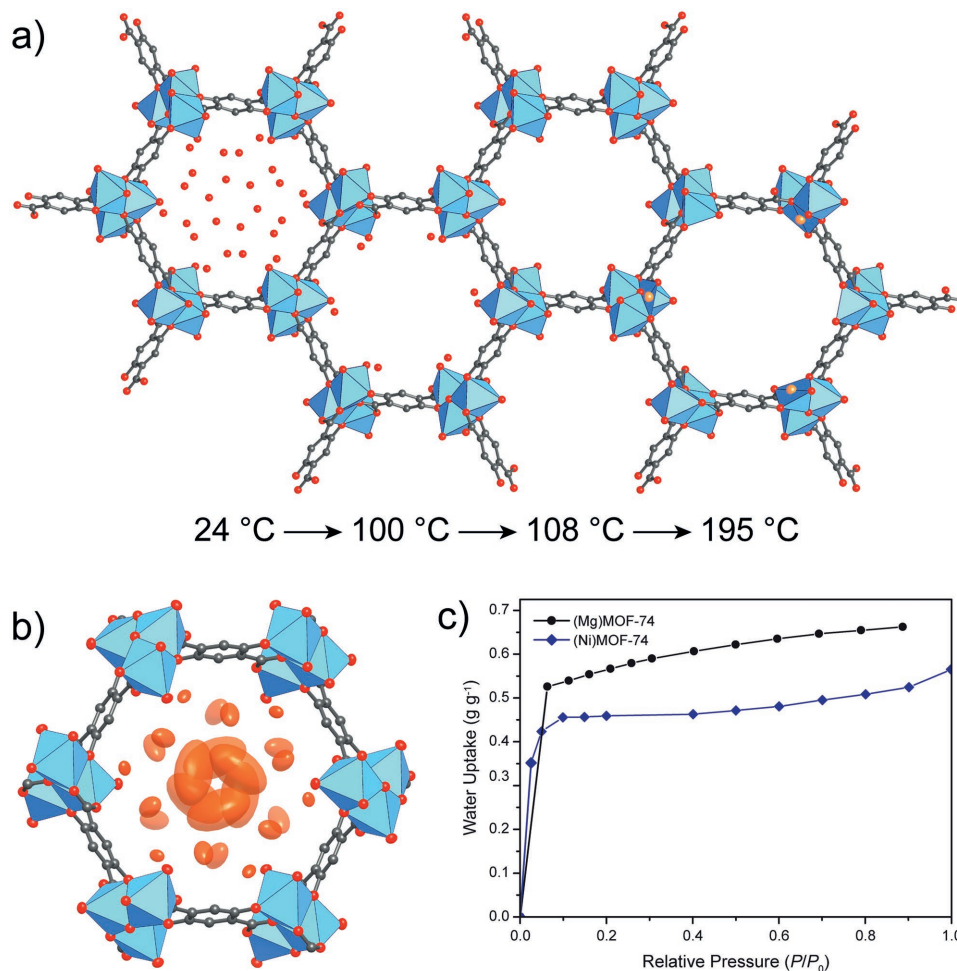

$$24\ °C \longrightarrow 100\ °C \longrightarrow 108\ °C \longrightarrow 195\ °C$$

Figure 6. Distinct dehydration steps in the structure of (Zn)MOF-74 determined by XRD measurements. a) Loosely bound water in the center of the pore is removed under mild conditions (24–100 °C), strongly adsorbed water is removed at 108 °C, and water chemisorbed on the SBUs is removed at high temperature (195 °C). b) Thermal ellipsoids of the different water molecules corresponding to the strength of their interaction with the framework.[52] c) The resulting water adsorption isotherm is of Type I, the difference in capacity between (Ni) and (Mg)MOF-74 is due to the difference in formula weight.[34c,67]

that are strongly physisorbed close to the SBUs, have larger thermal ellipsoids, and those located loosely in the center of the pore have the largest thermal ellipsoids. Three dehydration steps were found upon heating of MOF-74 which is in good agreement with the strength of the interactions for the three distinct adsorption sites (see Figure 6a). The high thermal energy required to regenerate (M)MOF-74 materials to their full capacity is related to the strong binding of water to the open metal sites of the SBU. Such high regeneration temperatures (195 °C for (Zn)MOF-74) are undesirable for most applications based on adsorption–desorption cycles. The strong binding between water and the open metal sites results in a large value of the Henrys constant K_H and a Type I isotherm (Figure 6c). Typically, the adsorption and desorption of water on open metal sites is accompanied by local or global structural deformation which may result in gradual degradation of the material upon repeated cycling.[52] Such structural changes where observed for the dehydration of the SBUs in the structure of UiO-66.[25a,53] Heating to temperatures above 250 °C results in a loss of two water molecules from the $Zr_6O_4(OH)_4(COO_2)_{12}$ SBU, accompanied by a decrease in the coordination number of zirconium from 8 to 7 and a strong distortion of the cluster.

3.2. Water Cluster Formation

Physisorption of water in microporous, hydrophilic adsorbents is initiated by nucleation on primary adsorption sites and the growth of water clusters rather than single or multilayer adsorption.[7] The primary adsorption sites are typically close to polar, hydrophilic centers within the structure (e.g., SBUs). Water molecules adsorbed on these sites can act as additional adsorption sites, initiating the formation of water clusters as evidenced by the step shape of the isotherm. The reversible formation of water clusters in MOF-801 has been studied by X-ray single crystal and neutron powder diffraction.[7] MOF-801 crystallizes in an **fcu** topology and has two differently sized tetrahedral, as well as one octahedral pore with diameters of 4.8, 5.6 and 7.4 Å, respectively.[7,54] The combination of small pores and short fumarate linkers provides for a hydrophilic pore system. At low relative pressures, water is adsorbed in the two tetrahedral pores. The highest occupancy was found for adsorption sites that are located close to the −OH groups of the SBU (sites I and II). An additional adsorption site (site III) was found in one of the tetrahedral pores, where additional water is hydrogen bonded to three water molecules on site II forming a water cluster with an overall cubic geometry. At 100% RH water is also adsorbed in the octahedral cavity. The octahedral cavity itself does not have specific adsorption sites, but it was shown that water molecules adsorbed on site III in the tetrahedral pores facilitate the adsorption of water in the octahedral cavity of the framework by hydrogen bonding. These findings suggest the instigation of water adsorption by formation of small water clusters that eventually connect, leading to continuous pore filling, a mechanism similar to that established for porous carbons.[55] The different adsorption sites in the tetrahedral and octahedral pores of MOF-801 are shown in **Figure 7**.

3.3. Capillary Condensation

In contrast to the reversible, cluster mediated pore filling mechanism found in hydrophilic microporous MOFs such as MOF-801, adsorption by capillary condensation is an irreversible (hysteretic) process. It is observed for materials with effective pore diameters larger than the critical diameter (D_C) for capillary condensation as calculated according to Equation (3)

$$D_C = \frac{4\sigma T_C}{(T_C - T)} \tag{3}$$

where σ is the van der Waals diameter of the adsorbate, and T_C and T are the critical temperature of the adsorbate and the adsorption temperature, respectively. The critical diameter for water at 25 °C is $D_C = 20.76$ Å and capillary condensation is therefore commonly observed in mesoporous MOFs. The resulting "S"-shaped isotherm typically shows a hysteresis loop between the adsorption and the desorption branch (**Figure 8**a,b). A hysteresis loop between the adsorption and desorption branch observed for MOFs with pore size smaller than 20 Å cannot be assigned to irreversible capillary condensation but it is commonly caused by structural deformation of the framework as a result of host–guest interactions, structural degradation of the MOF, or the formation of water superclusters.[56]

MIL-101 has a hierarchical pore system with two accessible pores of 29 and 34 Å diameter and pore openings of ≈12 and ≈16 Å, respectively. It displays an adsorption isotherm of the expected "S"-shape with two distinct steps. A low uptake is recorded at low relative pressures followed by a steep step at around $P/P_0 = 0.4$ and a second step at $P/P_0 = 0.5$, corresponding to filling of the smaller and larger pore, respectively (Figure 8b).[57] The strong hysteresis loop is indicative of capillary condensation. Nucleation and growth on the inner surface initiates the adsorption at low relative pressures, followed by capillary condensation at relative pressures larger than $P/P_0 = 0.4$. High heats of adsorption at low coverage (≈−80 kJ mol⁻¹) that decrease at a coverage of about 20% by almost 50% (≈−45 to −50 kJ mol⁻¹, a value close to the evaporation enthalpy of water) support this assumption.[58]

4. Single Component Water Adsorption Isotherms

The shape of a water adsorption isotherm gives important information on the predominant adsorption mechanism as well as on the strength of the interaction between the adsorbent and the adsorbate. All water adsorption isotherms discussed in this section are measured at 298 K unless specified otherwise. The gravimetric uptake (g g⁻¹) is plotted against the relative pressure given as P/P_0 where P_0 is the bulk saturation vapor pressure at 298 K. The relative pressure is equivalent to the relative humidity (RH, in %) at the specified temperature. Four quantities are commonly used to describe the water adsorption isotherm: (i) the water adsorption capacity (q_{max} in g g⁻¹), (ii) the relative pressure α at which half of the total capacity is reached (i.e., the inflection point of the isotherm), (iii) the Henry's constant K_H (i.e., the slope of the isotherm at low values of P/P_0), and (iv) the heat of adsorption (Q_{st} in kJ mol⁻¹).[59] In this review, only hydrophilic MOFs are discussed.
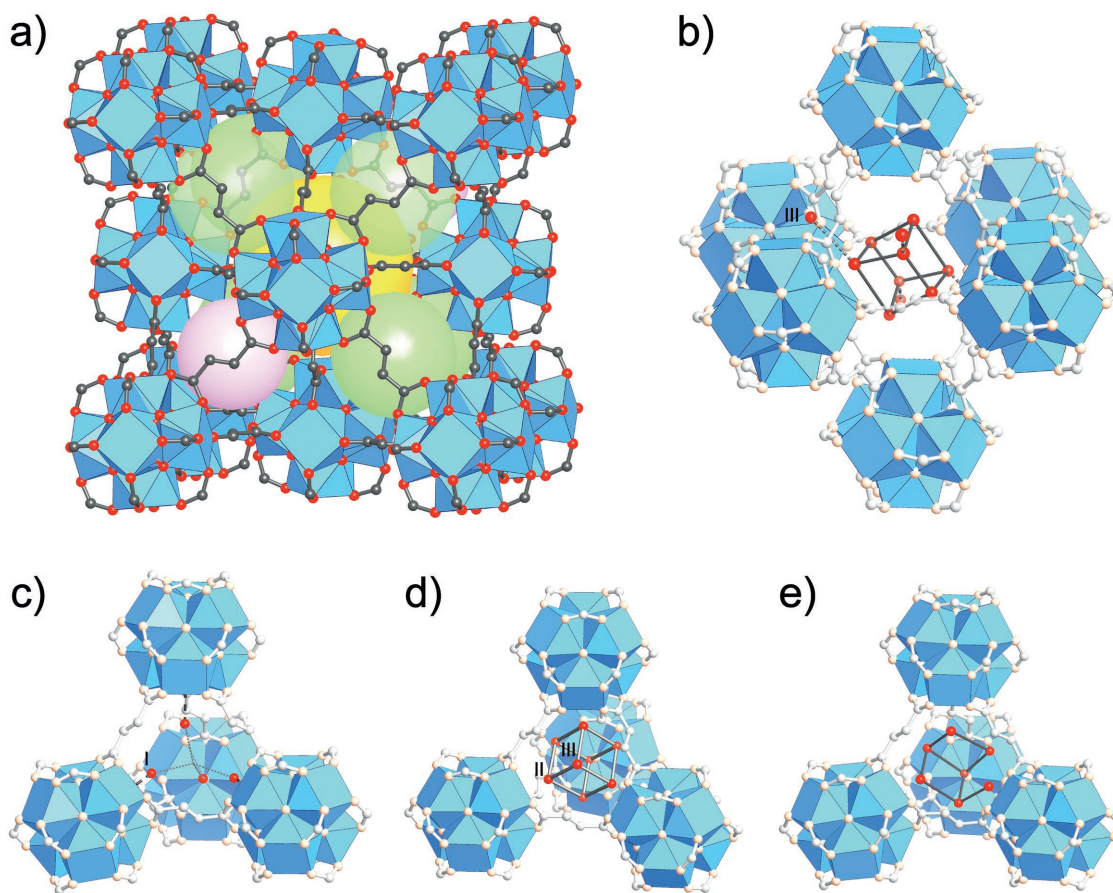
Figure 7. a) Single-crystal structure of MOF-801 illustrating three different cavities, two of which are tetrahedral (green and pink spheres) and one of which is octahedral (yellow sphere). c,d) Initial water adsorption upon exposure to humidity occurs through hydrogen-bond formation to the SBUs (site I and II) and among adsorbed water molecules (site III) as determined by single-crystal diffraction. e) Crystals exposed to increased levels of humidity (100% RH) show similar arrangements as well as incomplete cubic clusters. b) Adsorption of water in the octahedral cavities occurs through formation of hydrogen bonds with sites III.[7]

The maximum capacity of such materials is linked to the pore volume. The position of the inflection point α ($0 < \alpha < 1$) strongly correlates with the hydrophilicity of the pores and therefore to some extend also the pore size. The value of α decreases with increasing hydrophilicity allowing for the comparison of the relative hydrophobicity of isostructural MOFs. Since strong adsorption at low relative pressures close to zero (e.g., due to the presence of open metal sites) is unfavorable for water harvesting applications, only MOFs with low values of K_H are discussed. Where possible, these factors will be given to allow for a direct comparison of different materials based on their water adsorption isotherms. The materials discussed in this section are divided into mesoporous, microporous, and flexible/breathing MOFs. Chemical modifications influencing the adsorption behavior as well as composite materials aiming at large-scale applications will be discussed.

4.1. Water Adsorption Isotherms of Mesoporous MOFs

Water sorption isotherms of mesoporous MOFs are typically of Type IV or V and show a hysteresis loop due to capillary condensation. The MIL-100 [$M_3O(H_2O)_2(L)(BTC)_2$ where L = OH

or F] and MIL-101 series are among the most studied mesoporous MOFs. Even though their structures are built from linkers with different topicity, both structures have an underlying **mtn** topology. In both structures, tetrahedral tertiary building units (TBUs) are formed by linking trinuclear SBUs of trivalent metal cations (e.g., Cr^{3+}, Fe^{3+}, Al^{3+}) with ditopic BDC (MIL-101) or tritopic BTC (MIL-100) linkers. These TBUs are further linked to form two differently sized cages of 25 and 29 Å, or 29 and 34 Å in MIL-100 and MIL-101, respectively.[39,60] Water adsorption experiments performed on highly stable MIL-100 and MIL-101 materials revealed steep uptakes at relative humidity ranging from 25% to 60%.[21,61] As can be expected considering the different free pore volumes of these structures, the maximum capacity of (Cr)MIL-100 is lower than that of (Cr)MIL-101, with up to 0.8 and 1.4 g g^{-1}, respectively.[21,61d] For both materials, different maximum loadings have been reported depending on the method of sample preparation.[62] However, all measurements show similar 'S'-shaped adsorption isotherms with $\alpha \approx 0.46$ for (Cr)MIL-101 and $\alpha \approx 0.32$ for (Al)MIL-100 (Figure 8a,b).[61a,b] Water uptake at lower relative pressures is limited by the hydrophobicity of the organic linker, and uptake at relative pressures close
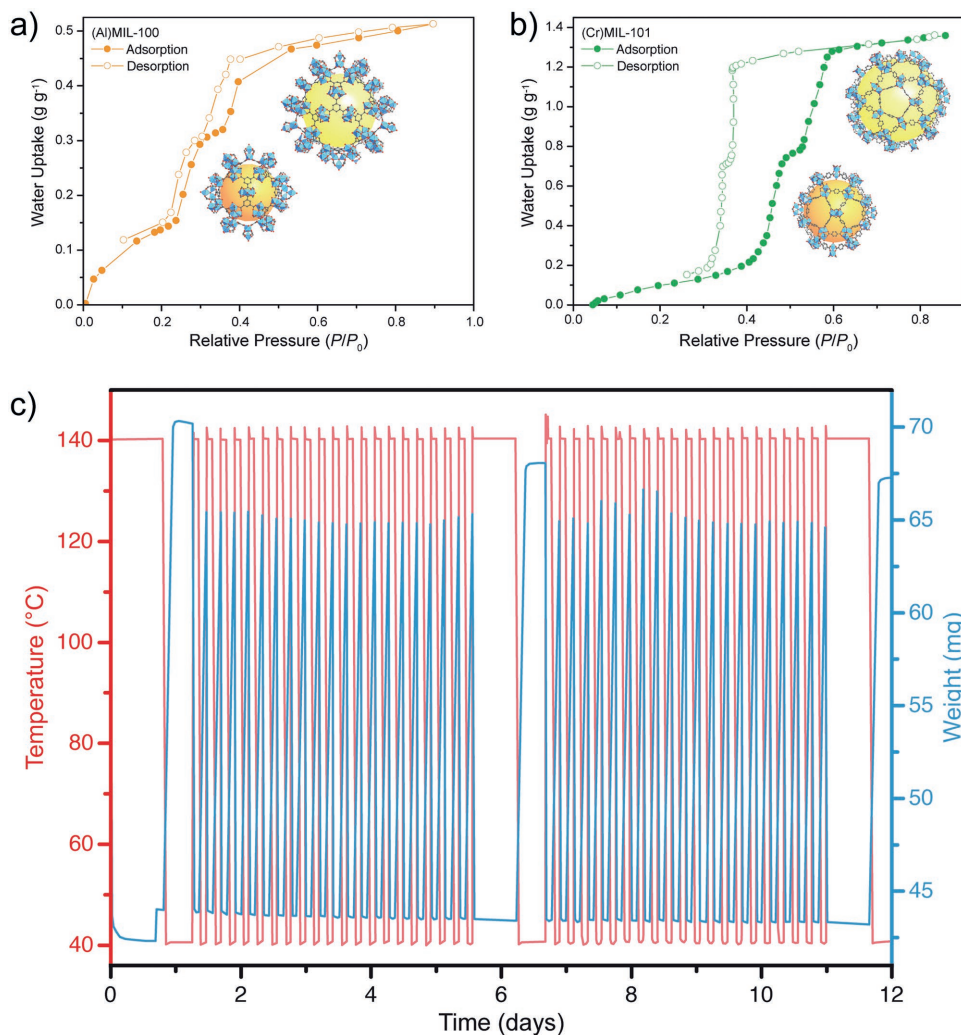
Figure 8. a,b) Water-sorption isotherms of (Cr)MIL-101 and (Al)MIL-100.[57,58] Two steps are observed corresponding to filling of the smaller and larger pore by capillary condensation. The hysteresis loop between the adsorption (filled symbols) and desorption (open symbols) branch is caused by the irreversibility of capillary condensation. c) Cycling experiments performed on (Cr)MIL-101 indicated a high performance-stability of the material with no significant loss in loading lift after more than 40 cycles.[63a]

to zero can mainly be ascribed to the presence of open metal sites in the fully activated material. At higher relative pressures two adsorption steps corresponding to the filling of the smaller and subsequently also the larger pore by capillary condensation are observed.[57] Water adsorption isotherms for both materials show a hysteresis between the adsorption and desorption branch due to irreversible capillary condensation. Owing to their outstanding water stability, the cycling stability of MIL-100 and MIL-101 materials has been extensively studied in the context of adsorption-driven heat pumps, room chillers, and sea water desalination, revealing a high performance-stability of these materials.[58,63] MIL-100 and MIL-101 materials have been demonstrated to be superior to traditional water adsorbents such as NaX [$Na_{86}(AlO_2)_{86}(SiO_2)_{106}$], SAPO-34 [$(SiO_2)_x(Al_2O_3)_y(P_2O_5)_z$], or silica gel in terms of water uptake and adsorption–desorption kinetics.[63a] Water adsorption isotherms and cycling experiments of (Al)MIL-100 and (Cr)MIL-101 are shown in Figure 8a–c.

The effect of functional groups on the water adsorption properties of MIL-101 was studied by partial incorporation of chemically modified linkers bearing functional groups capable of interacting with water.[57,64] The BDC linker in (Cr)MIL-101 was partially functionalized with $-COOH$ (**1**), $-NH_2$ (**2**), $-NHCONHCH_2CH_3$ (**3**), $-NHCOCHCHCOOH$ (**4**), and $-NH(CH_2)_3SO_3H$ (**5**). Water adsorption isotherms showed that incorporation of hydrophilic groups (**1**, **2**, **4**, **5**) shifts α to lower values ($\alpha = 0.42, 0.38, 0.40$, and 0.33, respectively) whereas hydrophobic groups (**3**) result in higher values of α ($\alpha = 0.58$) relative to the pristine (Cr)MIL-101 ($\alpha = 0.46$) (**Figure 9**a–f). The maximum capacity however decreased for all substituents which can be explained by a smaller free pore volume of the functionalized materials as evidenced by nitrogen adsorption isotherms. Hydrophilic functional groups attached directly to the hydrophobic linker show the lowest decrease in capacity while shifting the inflection point to lower relative pressures. The hydrophilicity of a given functional group is correlated to
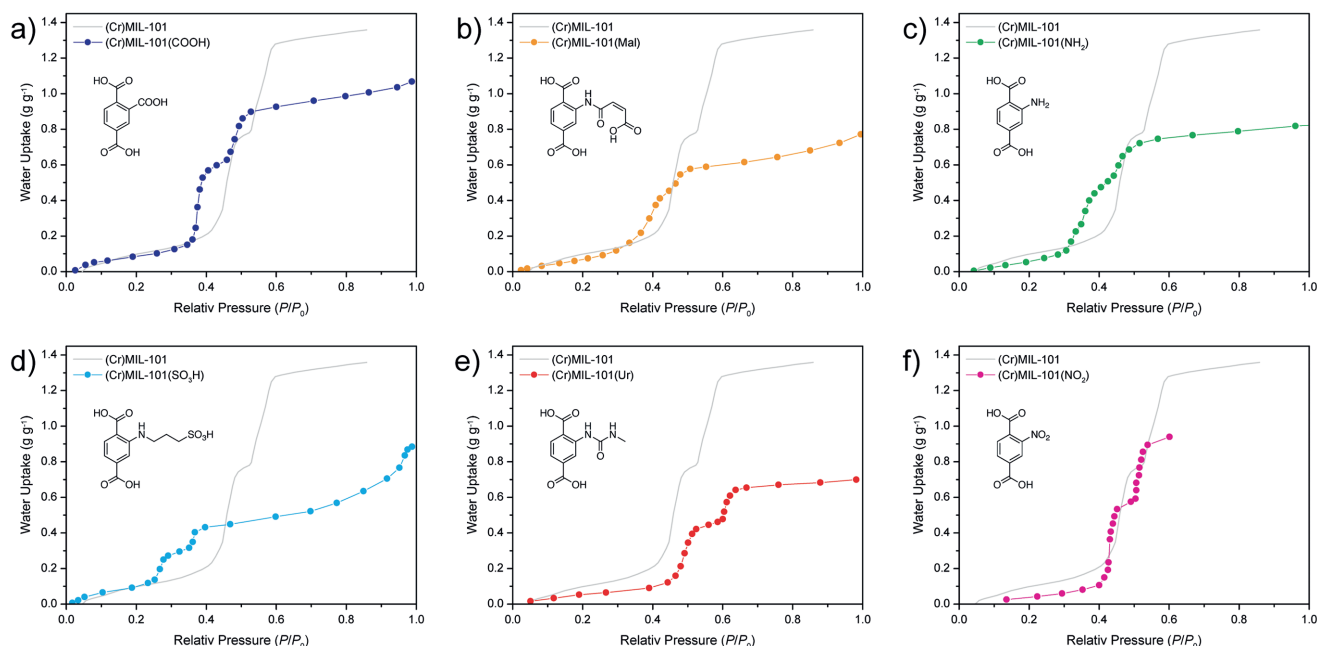
ADVANCED
SCIENCE NEWS
www.advancedsciencenews.com

ADVANCED
MATERIALS
www.advmat.de

Figure 9. Adsorption isotherms of functionalized (Cr)MIL-101 derivatives. Only the adsorption branch is shown, the isotherm of parent (Cr)MIL-101 is shown in light gray. Hydrophilic substituents shift the inflection point of the isotherm lower (a–d), hydrophobic groups to higher P/P_0 values (e), and hydroneutral groups have a negligible effect on the position of the inflection point (f). In all cases substitution leads to a decrease in maximum capacity, arguably due to the decreased pore volume.[57,64]

its donor- and hydration number, its pK_a, and its ability to act as a hydrogen bond donor or acceptor, rather than its dipole moment.[65] Therefore, functional groups such nitro groups, esters, and ketones are considered hydroneutral rather than hydrophilic. Higher loadings of functional groups were shown to neither increase the maximum capacity nor the uptake at low pressures compared to lower loadings. Appending −NO$_2$ substituents to the BDC linker in (Cr)MIL-101 showed that the hydroneutral −NO$_2$ substituent has a negligible effect on α but decreases the stability of the framework due to the electron withdrawing properties of −NO$_2$ (Figure 9).[61d,66]

4.2. Water Adsorption Isotherms of Microporous MOFs

Water adsorption isotherms of microporous hydrophilic MOFs can be of different types (e.g., Type I, II, IV) depending on the chemical nature of the MOF. Typically, no hysteresis is observed unless the adsorption of water results in a distortion, structural change, or degradation of the framework, or open metal sites are present. The adsorption of water in nickel and magnesium MOF-74 have been reported.[34c,67] Both compounds show a Type I adsorption isotherm similar to that commonly found in zeolites.[68] 81% of the maximum capacity is reached at very low relative pressures ($P/P_0 \approx 0.05$) which is ascribed to the presence of open metal sites.[62] The adsorption isotherms of (Ni) and (Mg)MOF-74 reach a plateau at $P/P_0 \approx 0.1$ and show a maximum capacity of 0.47 and 0.54 g g^{-1}, respectively (see Figure 6c).[34c,67] The lower gravimetric uptake of (Ni)MOF-74 compared to (Mg)MOF-74 is a consequence of its higher molar mass. (Ni)MOF-74 was shown to be a promising

candidate for water desalination in a two bed system operating at low evaporation (5 °C) and high regeneration temperature ($T \geq 110$ °C).[63a] The high regeneration temperature is required due to the strong interaction between the adsorbed water molecules and open metal sites, which makes MOF-74 materials irrelevant for water harvesting applications.

The water adsorption properties of CAU-10(H) [Al(OH)(m-BDC)$_2$] and a series of isostructural CAU-10 derivatives have been studied extensively. CAU-10(H) is built from fourfold helical rod-like SBUs of cis vertex-sharing AlO$_6$ octahedra, linked by ditopic, angled m-BDC linkers to form a framework of **yfm** topology with square 1D channels of 7 Å (**Figure 10**c).[69] The water sorption isotherm of CAU-10(H) is of Type V with a steep uptake at low relative pressures ($P/P_0 = 0.2$), in good agreement with both the pore size and hydrophilicity of the pores. Coatings of CAU-10(H) were shown to be very stable in the presence of water, retaining the initial capacity of 0.26 g g^{-1} after up to 10 000 cycles under the selected cycling condition.[70] The effects of functional groups appended to the m-BDC linker in the 5-position on the water sorption behavior of CAU-10 derivates have been extensively studied.[69b,71] Hydrophilic −OH substituents shift α to lower relative pressures, appended −NH$_2$ groups even change the general shape of the isotherm to a Type I isotherm. In contrast, hydroneutral and hydrophobic substituents (e.g., −NO$_2$, −CH$_3$) shift α to higher relative pressures. Appending functionalities was shown to result in a lower maximum capacity which is caused by the decrease in free pore volume. Replacement of m-BDC by 2,5-furane dicarboxylate (FDC) leads to the formation of MIL-160, a MOF isoreticular to CAU-10. The shorter, more hydrophilic FDC linker results in a material displaying a Type I isotherm with a slightly
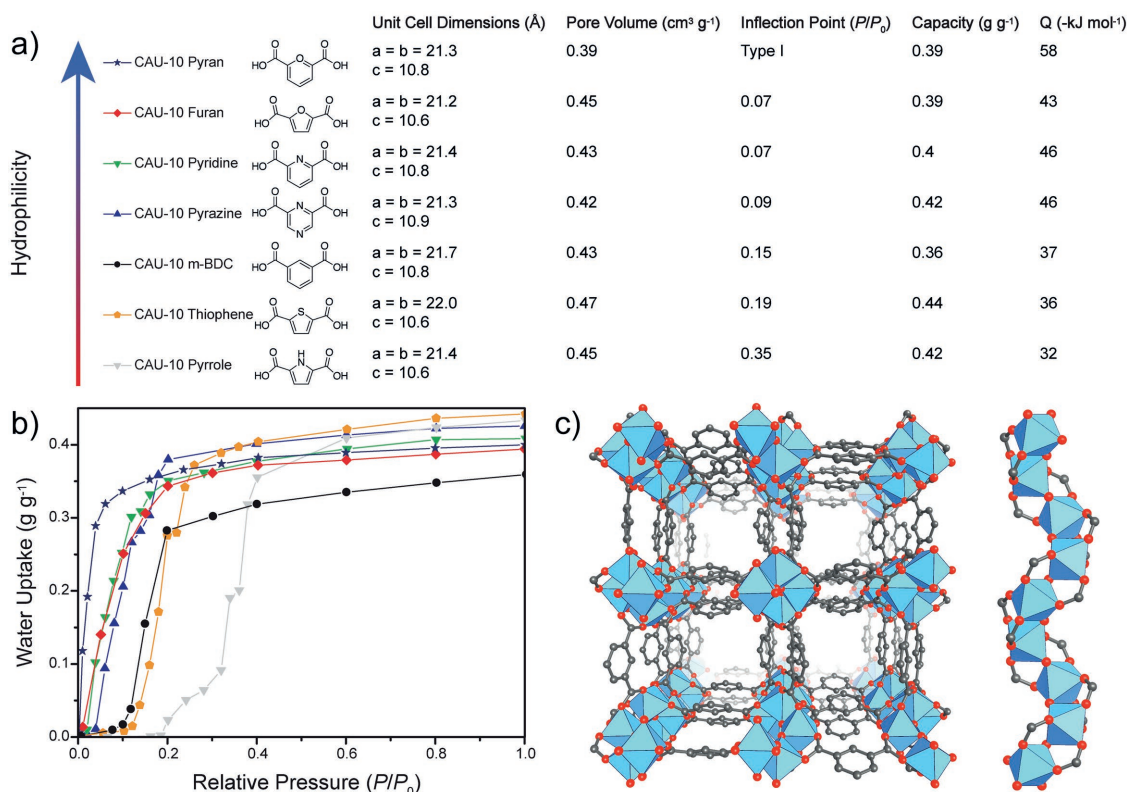
Figure 10. Comparison of structural parameters a) and water-adsorption isotherms b) of aluminum-based frameworks with **yfm** topology, isoreticular to CAU-10. c) The crystal structure of all materials is built from rod-like SBUs linked by bent ditopic linkers. The hydrophilicity of the linker influences the position of the inflection point of the isotherm, whereas the pore volume can be correlated to the maximum capacity of the material.[69,73]

increased maximum capacity as compared to the parent CAU-10(H). Grand canonical Monte Carlo (GCMC) calculations indicate that adsorbed water molecules interact preferentially with −OH groups bridging the metal centers in the rod-like SBUs. These findings were further supported by ^{1}H-NMR.[72] Recently, predicted isotherms for a series of (hypothetical) isoreticular MOFs based on CAU-10(H) were reported.[73] Furan, pyridine, pyrazine, and thiophene based linkers were demonstrated to improve the water affinity and adsorption capacity compared to CAU-10(H) considerably, while hydrophobic linkers (e.g. pyrrole) shift the inflection point to higher relative pressures. Considering that the pore volume and topology of all compounds reported in this study is similar, the inflection point can give information on the hydrophobicity of the pores. Figure 10 gives a comparison of structural parameters and (calculated) water adsorption isotherms of an isoreticular series of MOFs based on the structure of **yfm** net of CAU-10(H).

Unlike many other paddle wheel based MOFs, the mixed linker MOF ISE-1 [Ni$_3$(μ_3-BTC)$_2$(μ_4-BTRE)$_2$(μ-H$_2$O)$_2$, where BTRE = 1,2-bis(1,2,4-triazol-4-yl)ethane] was shown to be stable in the presence of water, with a high cycling stability.[74] The loading lift of 0.21 g g^{-1} does not decrease over 10 cycles under the chosen cycling conditions between 40 and 150 °C and 1.2 and 5.6 kPa. The high stability of ISE-1 renders it an interesting candidate for adsorption-based heat transformation applications such as refrigeration, heat pumps, and heat storage.

Since MOFs built from 12-connected Zr$_6$O$_4$(OH)$_4$ core SBUs typically show high water stability, many MOFs of this class are

of interest for water-adsorption-based applications. The adsorption mechanism of MOF-801 was discussed in Section 3.2. The water sorption isotherm of MOF-801 is of Type V with $\alpha \approx 0.08$. About 88% of the maximum capacity (0.36 g g^{-1}) is reached at $P/P_0 = 0.3$.[7] Single crystalline samples of MOF-801 show 78% of the capacity measured for powder samples. A similar trend was observed for nitrogen adsorption isotherms and the difference was attributed to a large amount of missing linker defects in the powder sample. MOF-801 was shown to have a high performance stability as indicated by the high cycling stability.[75]

The effect of isoreticular expansion on the water adsorption characteristics of MOFs with underlying **fcu** topology built from Zr$_6$O$_4$(OH)$_4$(COO)$_{12}$ SBUs allows for the delineation of general design principles for MOF suitable for water harvesting from air (**Figure 11**a). Increasing the length of the linker in MOF-801 renders the resulting MOF (UiO-66) more hydrophobic, leading to a shift of α to higher relative pressures ($P/P_0 = 0.36$ compared to $P/P_0 = 0.08$).[12,34c,76] The larger free pore volume manifests itself in a higher maximum capacity (0.44 g g^{-1}) compared to MOF-801 ($q_{max} = 0.36$ g g^{-1}) (Figure 11b, left). The effects of functionalization with hydrophilic and hydrophobic substituents appended to the BDC linker have been studied.[76b,77] The functionalization of BDC with one hydrophobic methyl substituent was shown to have no effect on the inflection point of the isotherm but leads to a lower maximum capacity due to the smaller free pore volume. A second methyl substituent appended to the BDC linker, however, not only resulted in a dramatic decrease of the maximum capacity
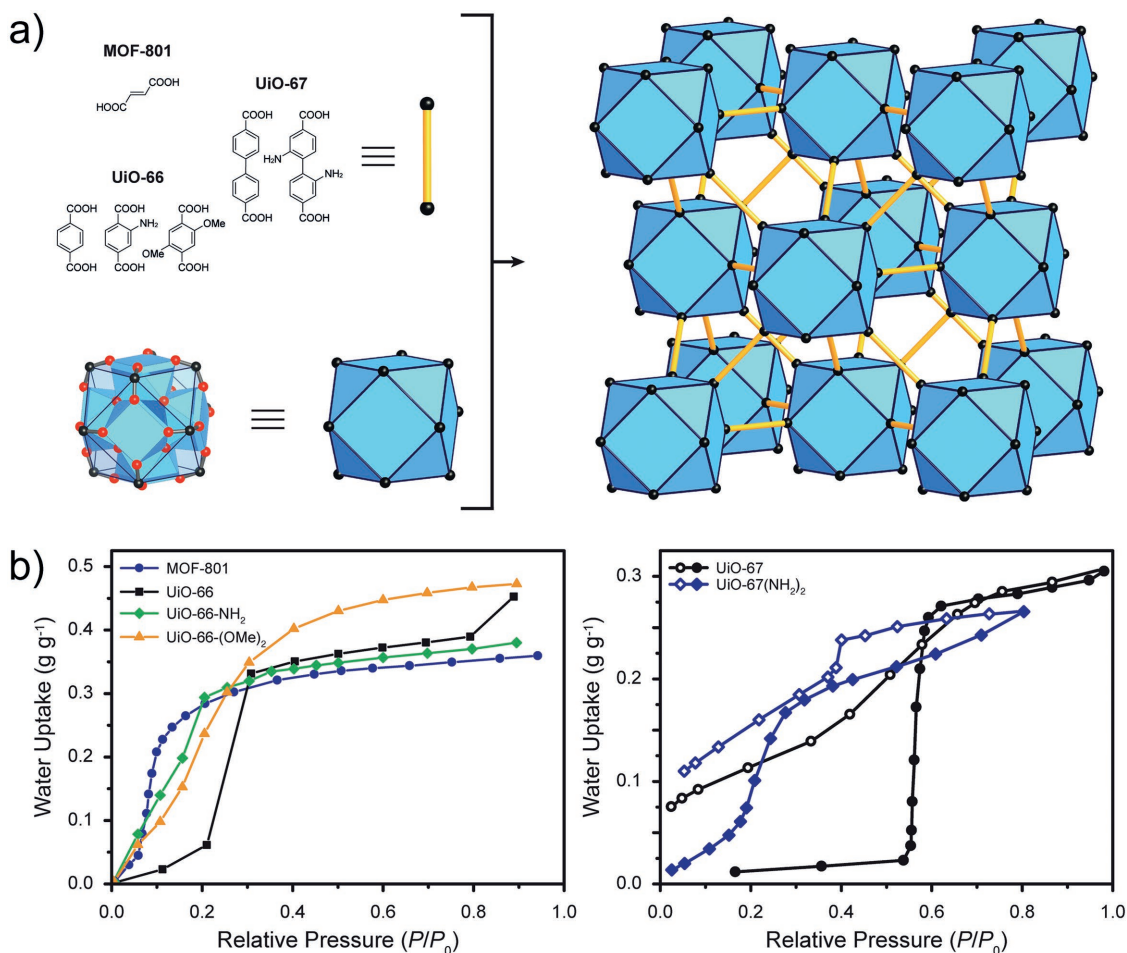
Figure 11. a) Isoreticular series of MOFs with **fcu** topology. The adsorption characteristics are highly dependent of the length and chemical nature of the linker. b) The difference in pore size between UiO-66 and MOF-801 results in different maximum capacities. A clear influence of the hydrophilicity of the linker is seen in the position of the inflection point of the isotherms. c) Hydrophilic −NH$_2$ substituents appended to the BPDC linker in the structure of UiO-67 result in a dramatic shift of the inflection point to lower relative pressures. The observed hysteresis is in good agreement with the presence of mesopores (octahedral cavities) within the material. The filled symbols represent the adsorption, open symbols the desorption.[7,76b,78]

but also an almost linear isotherm indicative of strong hydrophobicity. The inflection point of the Type V isotherm of hydrophilic UiO-66(NH$_2$) and hydroneutral UiO-66(NO$_2$) are shifted to lower relative pressures $P/P_0 = 0.15$, whereas hydrophilic UiO-66(OMe)$_2$ has a Type I isotherm and surprisingly displays the highest uptake among all UiO-66 derivatives (Figure 11b, left). Further expansion of the BDC linker by one aryl unit leads to the isoreticular UiO-67. This expansion results in a dramatic decrease of the capacity by 34% and a shift of the inflection point to $P/P_0 = 0.56$ along with a strong hysteresis, indicating structural degradation, and a higher hydrophobicity of the pores compared to UiO-66.[78] Appending two −NH$_2$ groups to the BPDC linker in UiO-67 was shown to afford more hydrophilic pores ($\alpha = 0.2$) while the capacity was decreased by only 10% (Figure 11b, right).

MOF-841 [Zr$_6$O$_4$(OH)$_4$O$_4$(MTB)$_2$(HCOO)$_4$(H$_2$O)$_2$], where MTB = methane tetrabenzoate] and DUT-67 [Zr$_6$O$_4$(OH)$_4$O$_4$(TDC)$_4$(HCOO)$_4$] are both built from 8-connected Zr$_6$O$_4$(OH)$_4$ core SBUs linked by tetratopic MTB or ditopic TDC linkers to form frameworks of **flu** and **reo** topology,

respectively.[7,25b] Both materials possess relatively similar pore volumes ($V_{p(MOF-841)} = 0.53$, $V_{p(DUT-67)} = 0.6$) and density ($d_{cryst(MOF-841)} = 1.05$, $d_{cryst(DUT-67)} = 1.06$) resulting in similar maximum capacities of 0.51 and 0.50 g g^{-1}, respectively. The small pores in MOF-841 (9.2 Å) are hydrophilic as evidenced by a low inflection point of the Type V isotherm at $P/P_0 = 0.24$. DUT-67 has a hierarchical pore system (11.7 and 14.2 Å) and the resulting Type IV isotherm therefore displays a stepwise uptake, where the first step is related to pore filling of the smaller, more hydrophilic ($\alpha = 0.26$) and the second step to pore filling of the larger, more hydrophobic pore ($\alpha = 0.37$). The isoreticular expanded version of DUT-67 (DUT-51) displays no steps in the Type IV isotherm regardless of the hierarchical pore system (15.6 and 18.8 Å).[31b] The larger, more hydrophobic pores in DUT-51 result in a higher maximum capacity of 0.54 g g^{-1} and a significant shift of the inflection point to higher relative pressures ($\alpha = 0.64$).

The preceding examples illustrated that the water sorption behavior of microporous MOFs is largely governed by the hydrophilicity of the pores, the free pore volume, and the pore diameter. In order to facilitate water adsorption following
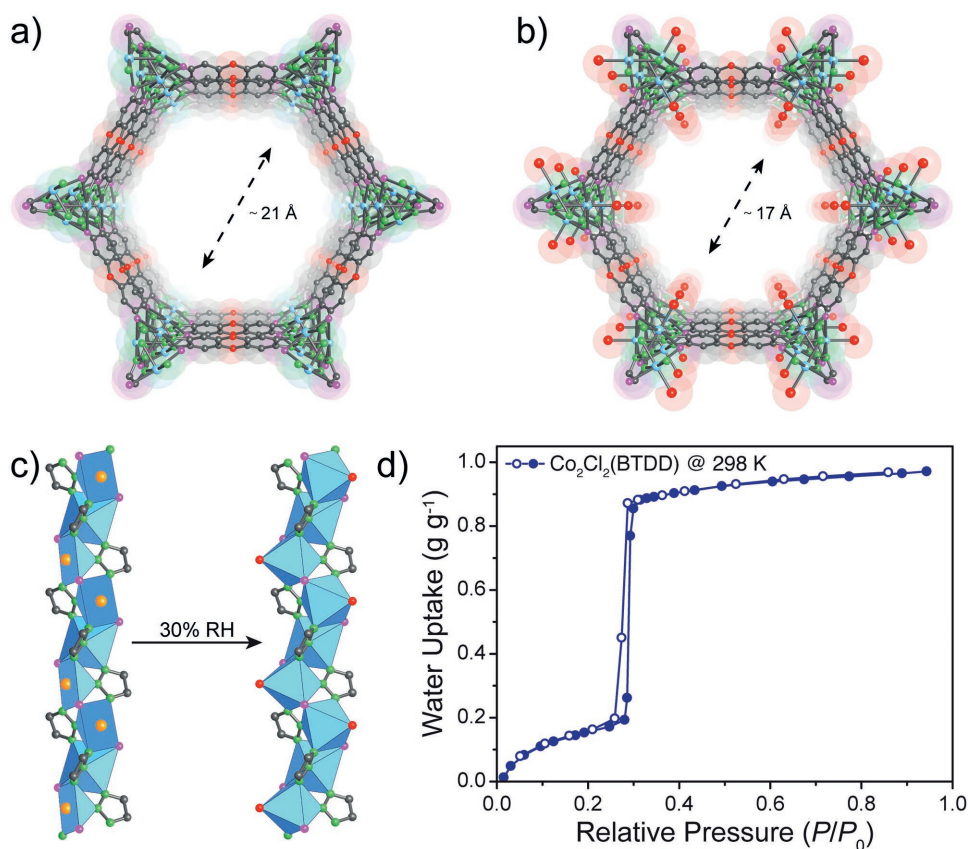
ADVANCED
SCIENCE NEWS
www.advancedsciencenews.com

ADVANCED
MATERIALS
www.advmat.de

Figure 12. 1D pores of fully activated a) and partially hydrated b) $Co_2Cl_2(BTDD)$. c) Rehydration of the open metal sites on the rod-like SBU at 30% RH decreases the effective pore size to about 17 Å, rendering reversible micropore filling the predominant mechanism for water adsorption. d) The Type IV water adsorption isotherm displays a steep uptake around $P/P_0 = 0.29$ and no hysteresis is observed. The filled symbols represent the adsorption, the open symbols the desorption.[11]

a pore filling mechanism, a pore diameter < 20.76 Å, the critical diameter D_C for capillary condensation of water at 25 °C, has to be maintained (see Equation (1)). Large working capacities within the range of 10–30% RH can therefore be expected for highly porous, hydrophilic, microporous MOFs with pore diameters approaching this value. The structure of the recently reported MOF $Co_2Cl_2(BTDD)$ contains hexagonal 1D channels of 21 Å diameter with open metal sites located on the rod-like SBUs, pointing at the center of the pores (**Figure 12**a).[11] The pore diameter suggests capillary condensation to be the predominant mechanism for water adsorption (at 25 °C). However, at low RH, the open metal sites in $Co_2Cl_2(BTDD)$ adsorb water, thereby decreasing the effective pore diameter to about 17 Å (Figure 12b,c). The water sorption isotherm of $Co_2Cl_2(BTDD)$ is of Type IV and shows a steep uptake at low relative pressures with an inflection point at $P/P_0 = 0.29$, ascribed to micropore filling. The high uptake at low relative pressures is a result of the polar, hydrophilic nature of the BTDD linker. The isosteric heat of adsorption (Q_{st}) during pore filling (−45.8 kJ mol^{-1}) is close to the evaporation enthalpy of water (−40.7 kJ mol^{-1}) indicating that water–water interactions are predominant during pore filling while the initial Q_{st} value at zero coverage (−55 kJ mol^{-1}) indicates strong interaction with the framework. These findings predict a facile regeneration of $Co_2Cl_2(BTDD)$ under mild conditions. $Co_2Cl_2(BTDD)$ has one of the highest reported water

adsorption capacity of 0.97 g g^{-1}, which in combination with the low value of α renders $Co_2Cl_2(BTDD)$ an interesting candidate for water harvesting (Figure 12d). Cycling studies under typical desert climate conditions of 5% RH at 45 °C and 35% RH at 25 °C corresponding to day and night, respectively, showed that the initial capacity of 84.7 wt% was decreased by 5.1 wt% after 6 cycles.

Even though not typically observed, the appearance of hysteresis loops in the isotherm of microporous materials arising from a specific adsorption mechanism has been reported. The structure of Y-**shp**-MOF-5 [$Y_9(\mu_3$-$O)_2(\mu_3$-$OH)_{12}(OH)_2(H_2O)_7(BTEB)_3(DMA)_3$, where BTEB = 1,2,4,5-tetrakis(4-carboxyphenyl)benzene] is built from 12-connected nonanuclear SBUs connected by ditopic BTEB linkers to form a framework of **shp** topology with trigonal channels of 12 Å diameter running along the crystallographic c-axis.[56b] Due to the hydrophobic nature of the pores, arising from the BTEB linker, the "S"-shaped Type-IV-like adsorption isotherm of Y-**shp**-MOF-5 shows an inflection point at high relative pressures ($P/P_0 = 0.64$), (**Figure 13**). Fully activated Y-**shp**-MOF-5 shows a low uptake of 5 wt% at low relative pressures ($P/P_0 < 0.2$), caused by the adsorption of water on the open metal sites of the SBU, after which a plateau is reached. A steep uptake is observed between $P/P_0 = 0.5$ and 0.75 before the full capacity of 50 wt% is reached (Figure 13). The uptake at high relative
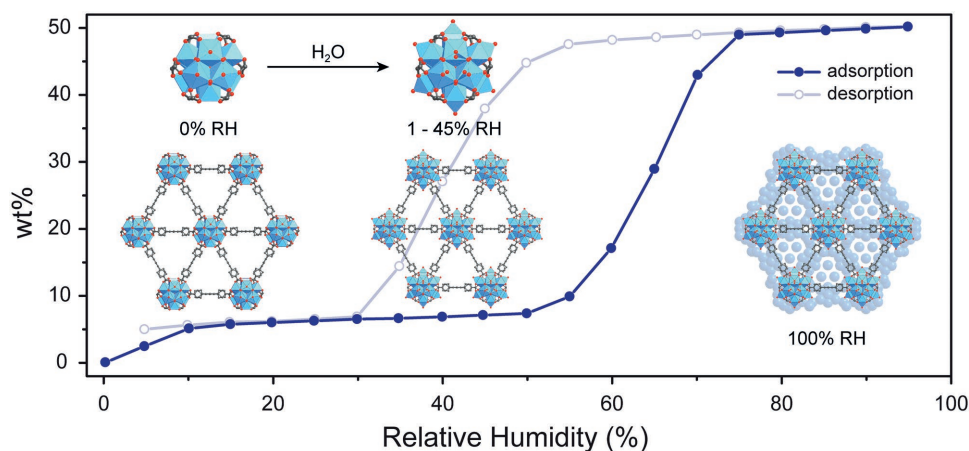
**ADVANCED
SCIENCE NEWS**

www.advancedsciencenews.com

**ADVANCED
MATERIALS**

www.advmat.de

Figure 13. Water-sorption isotherm of Y-shp-MOF-5.[56b] At 0% RH no water molecules are observed in the single-crystal structure of Y-**shp**-MOF-5 (left). Between 1% and 20% RH the open metal sites chemisorb water (middle) until a plateau is reached. Above 55% RH superclusters form in the triangular channels until the maximum capacity of 50 wt% is reached (right). The strong hysteresis is explained by the strong hydrogen bonding within the water superclusters.

pressures was rationalized by the formation of superclusters resulting from the connecting of small water clusters formed by adsorption on secondary adsorption sites at sufficiently high relative pressures, which results in instantaneous pore filling. Upon regeneration of Y-**shp**-MOF-5 at 25 °C a 10% decrease in capacity is observed due to the strong binding of water to the open metal sites. Interestingly, a strong hysteresis of the desorption branch is observed. This hysteresis is not related to structural changes or degradation, which is supported by the finding that after cycling Y-**shp**-MOF-5 for more than 200 cycles between 25% and 85% RH all structural features as well as the initial adsorption properties were maintained. Instead, this behavior is attributed to the presence of water superclusters in the pores. A large driving force is required in order for them to dissociate into smaller clusters held together by weaker dispersion forces.[79] The formation of superclusters is highly dependent on the pore structure and cannot be easily predicted.

4.3. Water Adsorption Isotherms of Flexible MOFs

Several examples of MOFs exhibiting a structural deformation upon gas adsorption have been reported.[10a,56a,80] Here, breathing refers to a reversible structural phase transition upon adsorption or desorption, resulting in a breathing-like motion of the framework, whereas gate-opening refers to an abrupt structural transition of a material from a narrow pore (*np*) to a wide pore (*wp*) phase at a nonzero pressure. Breathing or gate-opening effects cannot be identified from the adsorption isotherm alone, since other effects such as degradation, change in adsorbate packing, or the transition from monolayer adsorption to pore filling can result in similarly shaped adsorption isotherms. Therefore, crystallographic evidence is needed in order to confirm flexible behavior. One of the first examples of a MOF exhibiting breathing behavior, that was studied by in situ XRD techniques, is MIL-53, a MOF built from infinite rod-like SBUs linked by ditopic BDC linkers to form a framework of **sra** topology with 1D channels of 8.5 Å diameter.[10b,81] It is assumed that the breathing

in MIL-53 is caused by the interaction of the framework with the dipole or quadrupole momentum of the adsorbate molecules.[82] Fully dehydrated samples of (Cr)MIL-53 show a transition from the thermodynamically stable, *wp* form into the *np* form upon exposure to air. Interestingly, isoreticular materials built from different metal ions show significantly different breathing behavior. Whereas the breathing motion in (Cr)MIL-53 leads to a change in unit cell volume of 40%, that in (Fe)MIL-53 causes an expansion of only 10%.[83] A detailed study of the energetics of breathing in (Al)MIL-53 and (Ga)MIL-53 revealed a thermodynamically stable *np* form for (Ga)MIL-53 which expands into an intermediate *np* form upon hydration.[84] The influence of functionalization on the water adsorption behavior of flexible MOFs is more difficult to rationalize than that of rigid MOFs. Studies on the influence of hydrophilic groups appended to the BDC linker in (Al) and (Fe)MIL-53 have been reported.[85] Whereas pristine (Al)MIL-53 displays a Type V isotherm ($\alpha = 0.28$), $-NH_2$ functionalized (Al)MIL-53(NH_2) displays Type I isotherms which is ascribed to the larger flexibility of pristine (Al)MIL-53.[86] The uptake of one molecule of water per metal unit corresponds to the hydrated structure where one water molecule per metal unit is located in the center of the 1D channel.[87] (Al)MIL-53(OH) displays a Type IV isotherm with a 500% increase in maximum capacity compared to pristine (Al)MIL-53. The steep uptake at high relative pressures ($\alpha = 0.8$) is a result of a structural transition from an *np* to a *wp* phase leading to a pronounced hysteresis loop between the adsorption and desorption branch. (Fe)MIL-53(COOH)$_2$ displays a Type I isotherm with a hysteresis loop, indicative of structural changes during the adsorption. The adsorption isotherms for (Al)MIL-53 derivatives and (Fe)MIL-53(COOH)$_2$ are given in **Figure 14**, the insets in Figure 14 illustrate the structural transition from the *np* to the *wp* phase of MIL-53 materials.

4.4. Water Adsorption Isotherms of MOF Composites

With respect to possible applications, monolithic shaping and the preparation of MOF films has recently gained more importance.
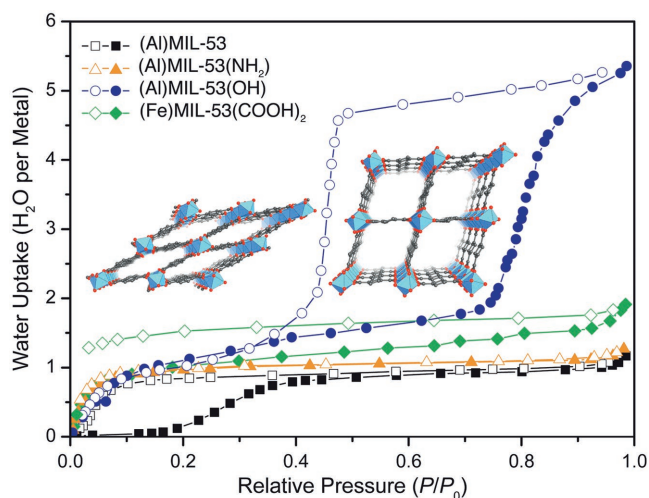
**ADVANCED
SCIENCE NEWS**

www.advancedsciencenews.com

**ADVANCED
MATERIALS**

www.advmat.de

Figure 14. Water-sorption isotherms for isoreticular (M)MIL-53(R) (M = Al, Fe; R = −(NH₂), −(OH), and −(COOH)₂) materials. Pristine (Al) MIL-53 (black squares) shows a Type V isotherm and strong hysteresis related to structural changes during the sorption process, whereas (Al) MIL-53(NH₂) (orange triangles) and (Fe)MIL-53(COOH)₂ (green diamonds) show Type I isotherms. (Al)MIL-53(OH) (blue circles) show a strong breathing effect at $P/P_0 = 0.8$ and a strong hysteresis between the adsorption and desorption branch. The structures shown correspond to the open and closed pore phases of (Al)MIL-53(OH). Closed symbols correspond to the adsorption, open symbols to the desorption of water.[85,86]

The preparation of monolithic xerogel composites from (Fe) MIL-100, (Cr)MIL-100, or (Cr)MIL-101 and mesoporous resorcinol-formaldehyde (R,F-xerogel) has been reported recently.[88] All monolithic bodies prepared in this study were shown to be mechanically stable and their gas uptake determined by N_2 adsorption was found to be close to the expected values according to the weight percentage of MOF within the composite materials.[88a] The general shape of the Type IV and V water sorption isotherms of MIL-100 and MIL-101, respectively, was not influenced (**Figure 15**). Water adsorption isotherms of 77 wt% (Cr)MIL-101 loaded R,F-xerogel composite displayed a slight shift of the inflection point toward lower relative pressure compared to pristine (Cr)MIL-101.

In another study the same MOFs were embedded into a macroporous oil-water (o/w) high internal phase emulsion (HIPE) foam, based on crosslinked poly(N-isopropyl acrylamide) (NIPAM).[88b] The pre-polymerization time of the HIPE
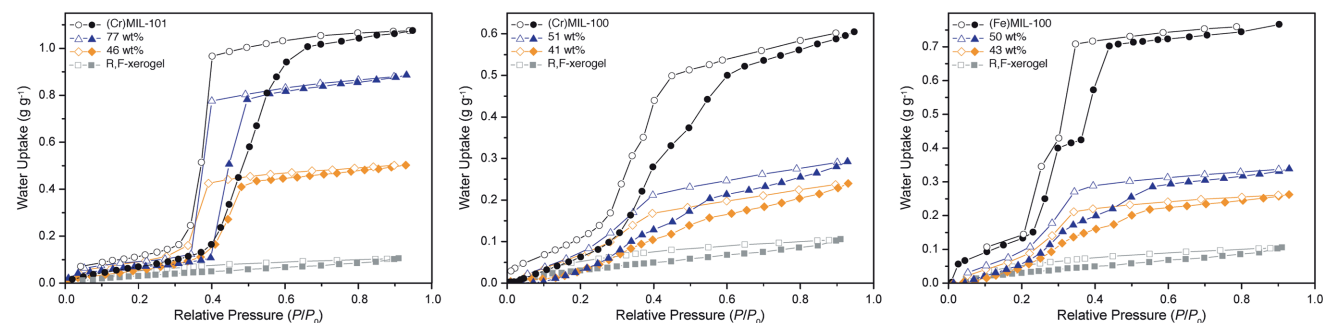
foam before the addition of MOF powders was shown to have a strong influence on the properties of the resulting materials. Pore blocking effects were minimized by virtue of optimizing the pre-polymerization time allowing for a loading of up to 92 wt% of MOF. All MIL@NIPAM composites displayed a higher water uptake than pure HIPE, however, a significant decrease in both surface area and maximum water adsorption capacity compared to pristine MIL-100 and MIL-101 samples was observed. (Cr)MIL-101(71 wt%)@NIPAM maintains the "S"-shape of the Type V water adsorption isotherm of MIL-101. In comparison to pristine (Cr)MIL-101, the inflection point is shifted to slightly lower pressures ($\alpha = 0.4$ compared to 0.46 for pristine (Cr)MIL-101) while the maximum capacity is reduced by 66% to 0.4 g g^{-1}.

Coatings of Al-fumarate (Al(OH)(fumarate), Basolite A520, BASF SE) embedded in a polysiloxane (SilRes MP50 E, Wacker Chemie AG) were tested on a full-size heat exchanger.[89] An even, highly stable coating of 300–330 µm thickness with an equilibrium loading of 0.317 g g^{-1} ($P/P_0 = 0.48$, adsorption at 30 °C, evaporator at 18 °C) and a corrected adsorption loading of 0.309 g g^{-1}, equaling 97% of that of the pristine material, was prepared by dip coating. Aside from the use in cooling systems, the low desorption temperatures below 65 °C, the low inflection point ($\alpha = 0.26$), the general shape of the Type V isotherm, the maximum capacity of 0.42 g g^{-1}, combined with the high hydrolytic stability render this material interesting for water harvesting. From an industrial point of view, the fast adsorption kinetics, compared to conventional adsorbents, the resulting cooling performance, the facile processability, and the cycle stability (95% after 360 cycles) make this composite coating suitable for large-scale applications.

Recently the application of MOFs in "composite salt in porous matrix" (CSPM) materials for the application in adsorption-based thermal batteries and chillers has been reported. $CaCl_2$ was encapsulated into (Fe)MIL-127 [Fe₃O(F)(H₂O)₂(ABTC)₁.₅, where ABTC = 3,3′,5,5′-azobenzene-tetracarboxylate], (Fe)MIL-100, (Cr)MIL-101, UiO-66(NH₂), (Ti)MIL-125(NH₂) [Ti₈O₈(OH)₄(NH₂-BDC)₆], and (Al)MIL-160 [Al(OH) FDC].[90] CSPM materials of UiO-66 and $CaCl_2$ (53 wt%) showed a specific cooling power of 631 W kg^{-1} and a coefficient of performance (COP) of 0.8; values comparable to the best solid adsorbents.

A recent study investigated novel composites of (Fe)MIL-100 and multiwalled carbon nanotubes (MWCNTs) prepared using a

Figure 15. Water-adsorption isotherms for R,F-xerogel composites of: a) (Cr)MIL-101, b) (Cr)MIL-100, and c) (Fe)MIL-100 for different loadings of MOF. The isotherms of the pure MOF phase are shown in black, that of the pure R,F-xerogel in gray. An uptake equal to that expected for the respective MOF content of the composite is observed in all cases.[88a]

**ADVANCED
SCIENCE NEWS**

www.advancedsciencenews.com

**ADVANCED
MATERIALS**

www.advmat.de

molecular-level mixing process.[88c] Composites containing varying volume fractions of MWCNTs were synthesized. Nitrogen adsorption measurements showed an increased BET surface area for a composite containing 10.72 wt% of MWCNTs. The characteristic Type IV isotherm of (Fe)MIL-100 is maintained and water adsorption isotherms showed a maximum uptake similar to pristine (Fe)MIL-100 with 38.77, 42.96, and 40.86 wt% for composites with 2.16, 5.90, and 10.72 wt% MWCNTs, respectively. Cycling stability tests revealed a stabilizing function of a low content (2.16 wt%) of MWCNTs. Such composite materials provide the opportunity to increase the coefficient of thermal conductivity while maintaining the adsorption characteristics of the MOF.

For the large-scale application of MOFs in water-adsorption-based processes, the use of powdered materials is not germane.[91] Hence, the above presented research on the preparation of composite materials allowing for facile production of films and monolithic bodies constitutes an important progression in transferring lab-scale results to large-scale applications. Embedding MOFs into polymer matrices appears to be a promising approach, even though it should be noted that efforts have been made to produce shaped bodies by pressing and extrusion on an industrial scale.[92] Polymer matrices appear especially promising since the water adsorption properties of the composite can be tuned through the hydrophilicity of the polymer. Whereas methods for the preparation of MOF-polymer composite films and shaped bodies are scarce, the fabrication of composite membranes has been studied in detail with respect to separation processes and will not be discussed in more detail.[93]

5. Water Harvesting From Air

The earths' atmospheric humidity equals about 10% of all liquid freshwater resources. In many arid regions of the world this constitutes the most abundant water source and adsorption-based water harvesting from air could therefore potentially address the global water problem. Many conventional porous materials (i.e., zeolites, porous silica, and porous carbons) suffer from two major drawbacks with respect to water harvesting applications: low maximum capacity and/or high regeneration temperatures. The ultrahigh porosity of MOFs combined with their wide structural diversity renders them promising candidates for adsorption-based water harvesting from air. The preceding sections pointed out that MOFs can combine large free pore volumes with the structural tunability needed for the precise adjustment of the strength of interactions with the adsorbate, facilitating the use of low grade energy sources such as solar or waste energy for combined PSA/TSA cycles. In this section the working principles of autonomous, low-energy water harvesting devices will be illustrated. Based on the demands with regard to the adsorbent a method for the selection of promising materials is proposed and design principles for next generation water adsorbents are outlined.

5.1. Working Principles of Water Harvesting

An ideal system for water harvesting should be powered by low grade, renewable, and abundant energy sources (e.g.,

solar–thermal heating), requiring materials with a large working capacity under these conditions. The water harvesting process in such devices consists of three steps: (i) adsorption of water from air at low temperatures and high RH, (ii) desorption at elevated temperatures, and (iii) condensation at low temperatures. This process can be illustrated using the psychrometric chart which provides a relation between the temperature and the humidity ratio for a given pressure. **Figure 16b** shows a psychrometric chart between −20 and 60 °C at sea level (760 mmHg or 1 atm) and Figure 16c depicts a schematic working cycle of a simple water harvesting device operating between 20 and 60 °C. The device consists of an enclosure equipped with a condenser and an adsorbent at opposing sites. The enclosure can be opened and closed to allow for a controlled exchange of the atmosphere (Figure 16d). The first step in the water harvesting cycle is the adsorption of water by the adsorbent. This is achieved by exposure of the adsorbent to cool, humid air (here 20 °C at 20% RH), typical values for the night in dry desert areas. When the adsorbent is saturated, the enclosure is sealed in order to create a closed system (Point 1, Figure 16b). When the temperature of the adsorbent is increased (e.g., by solar–thermal heating during the day), water is desorbed resulting in an increased humidity ratio of the air within the enclosure (red line, Figure 16b). The slope of the line connecting points 1 and 2 in Figure 16b is determined by the working capacity and the adsorption–desorption kinetics of the adsorbent. Subsequent cooling of the humid air on the condenser leads to an increase in the RH value until the dew point for the given temperature is reached (100% RH) and water starts to condense (Point 3, Figure 16b) which allows to collect the humidity adsorbed by the adsorbent as liquid water.

Recently an adsorption-based water harvesting device using MOF-801 has been reported.[75] The high water uptake of MOF-801 at low relative pressure region (0.29 g g^{-1} at α = 0.3 and T = 25 °C) renders it suitable for the application in water harvesting devices driven by low grade energy. A temperature swing of 40 °C is sufficient to fully regenerate MOF-801, restoring its initial capacity (see Figure 16a). The reported device is based on an enclosure that is equipped with one heated, MOF coated (adsorbent) and one cooled surface (condenser). A working cycle similar to that shown in Figure 16c was suggested. A TSA–PSA cycle between 25 and 65 °C allowed to harvest an extrapolated amount of 0.24 L of water per kilogram of MOF per day, as obtained by integration of the water harvesting rate, starting from air with 25 °C and 20% RH. A photograph of the passive device and the water droplets formed on the condenser upon increasing the temperature of the MOF are given in Figure 16d. This work provides an important proof-of-concept, demonstrating that harvesting water using only renewable solar–thermal energy is indeed possible and that further solutions based on this idea can eventually address the challenges of water production and distribution in arid, landlocked regions of this world, even in view of the increasing demand and decreasing supplies. The challenge of achieving this goal however requires both, advances in the design of next generation MOFs as well as elaborate engineering with respect to the design of passive water harvesting devices. The design of water harvesting devices is an engineering matter and basic considerations have been discussed elsewhere.[5d]
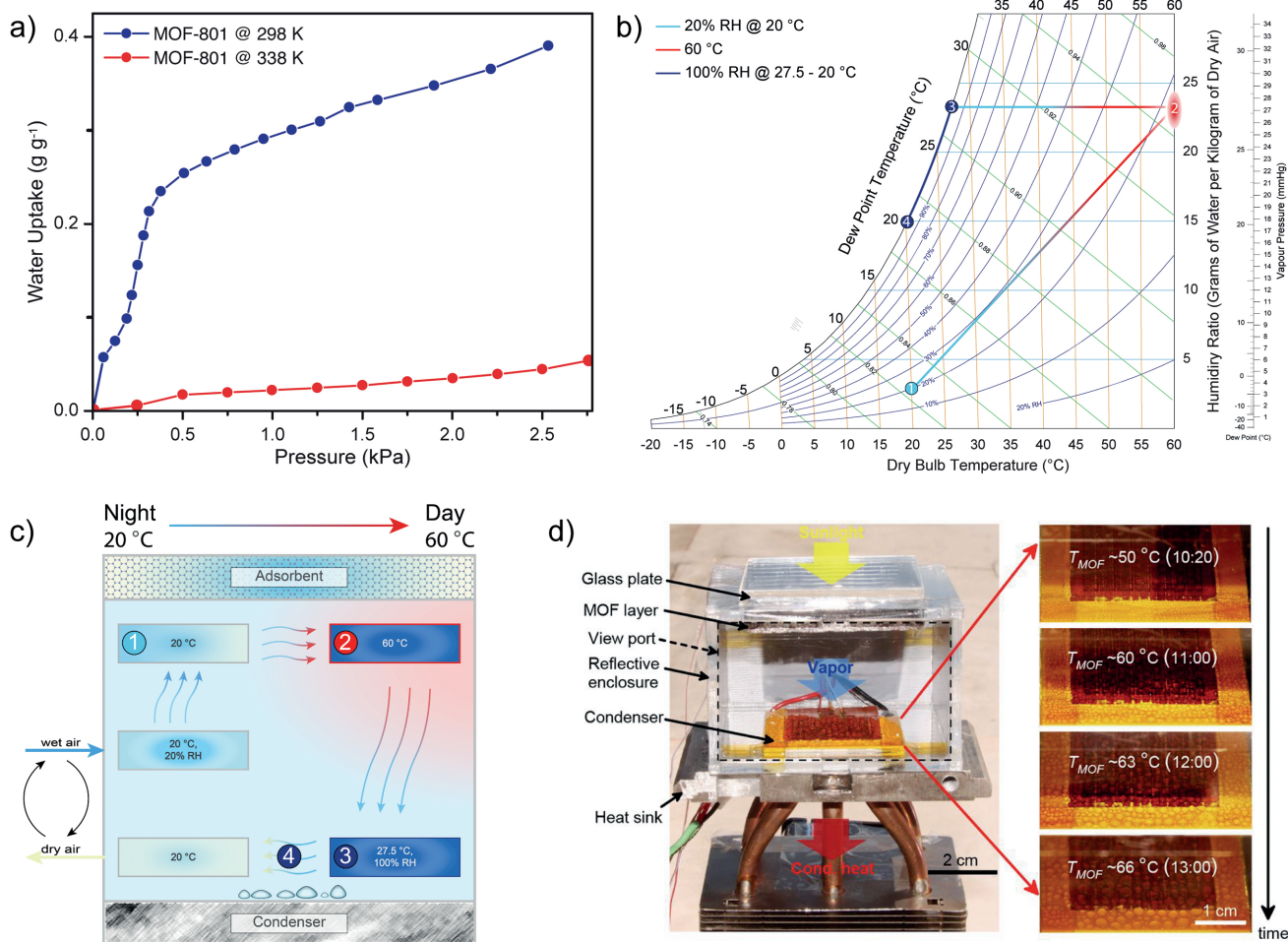
ADVANCED
SCIENCE NEWS
www.advancedsciencenews.com

ADVANCED
MATERIALS
www.advmat.de

Figure 16. a) Water-adsorption isotherms of MOF-801 recorded at 298 and 338 K. b) Psychrometric chart at sea level (760 mmHg) between −20 and 60 °C. c) Schematic of a passive water-harvesting device; steps in the process correspond to those highlighted in the psychrometric chart. The MOF is saturated with at 20 °C (20% RH, night conditions, point 1); subsequent heating during the day regenerates the MOF (point 2); the humidity ratio inside the device is increased until 100% RH is reached close to the condenser (point 3). Water condenses (point 4) and the dry air is exchanged by humid air again to close the cycle. d) Photograph of a passive water-harvesting device, the insert shows water droplets forming on the condenser upon increasing the temperature of the MOF adsorbent. d) Reproduced with permission.[75] Copyright 2017, AAAS.

5.2. Selection of Water Harvesting Materials

The selection of adsorbents for water harvesting is governed by several factors, the most important ones being: (i) the water stability, (ii) cycling stability, (iii) working capacity, (iv) pressure and/or temperature swing conditions, (iv) sorption kinetics, (v) thermal conductivity and spectral properties. The hydrolytic and cycling stability have been discussed earlier and this section is focused on the determination of the performance stability of MOFs with respect to water harvesting from air.

No standardized procedure for the selection of adsorbents for water harvesting has been established. In the following we present a rational approach to the evaluation and selection of water stable MOFs based on information gained from their isotherms and measurements of the adsorption–desorption kinetics in both TSA and PSA (see **Figure 17**). While it is evident that a large maximum capacity is required in order to facilitate efficient water harvesting from air, the pressure window in which

the uptake takes place is just as important. A steep uptake in a narrow pressure region between 10 and 30% RH (i.e., Type IV or V isotherm with a small value for α) is desirable since it facilitates water adsorption at low relative pressures (i.e., low RH), while allowing for regeneration of the initial capacity under mild conditions.[7] Traditional desiccants often either show significant water uptake at very low RH, even close to 0% RH, and therefore bind water too strongly (e.g., zeolites), or have a low uptake over a wide pressure range (e.g., silica gel), rendering them unsuitable for efficient adsorption-based water harvesting from air. Figure 17b shows schematic isotherms for three materials with different values of α. The inflection points of materials 1 and 2 are within the desired pressure region of $P/P_0 = 0.1$ and $P/P_0 = 0.3$, the uptake of material 3, even though steep, takes place at too high relative pressures to allow for water harvesting from dry air. **Figure 18** shows a comparison of the water uptake of different porous materials at $P/P_0 = 0.3$, 0.6, and 0.9. The working capacity under ideal temperature swing
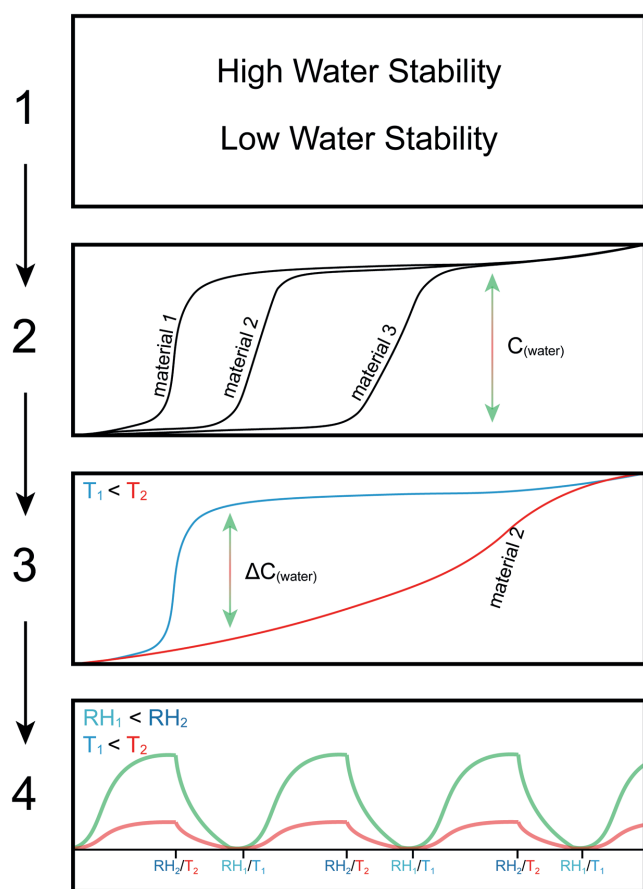
Figure 17. Flow chart for the selection of promising MOFs for water harvesting from air. a) High water stability is required in order to provide high cycling performance. b) The material should show a Type IV isotherm with a steep uptake ideally located between 10% and 30% RH. c) Isotherms recorded at temperatures between 25 and 65 °C should show significantly different profiles to allow efficient TSA. d) Sorption kinetics should be measured within different RH and temperature intervals to determine appropriate working conditions as well as the maximum loading lift under these conditions.

conditions should be determined by measurement of isotherms at different temperatures. An idealized set of isotherms at two different temperatures ($T_1 < T_2$) is shown in Figure 17c, where a large difference in capacity at low relative pressures is observed, allowing for efficient TSA within the temperature window $T_1–T_2$. The measurements carried out in steps 2 and 3 provide information on the maximum achievable loading lift in pure PSA and TSA cycles, respectively. Most designs of passive water harvesting devices will however operate based on combined PSA–TSA cycles.[75] The working capacity determined in idealized TSA and PSA cycles is often limited by the adsorption–desorption kinetics. Therefore, the fourth step in the selection process should consist of kinetics measurements within different pressure and temperature intervals. Only few studies of water adsorption–desorption kinetics for MOFs have been reported thus far. The kinetics of water adsorption in (Ni)MOF-74, commercial aluminum fumarate (Basolite A520, BASF SE) and (Cr)MIL-101 have been studied and numerical models have been established.[94] These models have been proven useful in

the optimization of operating parameters in adsorption based desalination processes such as the optimization of the heat source temperature.[63a] We suggest the selection of multiple pressure intervals for the determination of adsorption–desorption kinetics in a way that different adsorption mechanisms predominate within these segments, e.g., around the onset, inflection point and plateau of the area of steep uptake. Such measurements allow for the determination of the boundaries for ideal PSA conditions. Figure 17d illustrates a kinetics measurement where either the temperature or the relative humidity is varied in periodic intervals allowing for the determination of the working capacity at a fixed cycling rate. The kinetics measured on powder samples typically do not represent those of processed MOF (e.g., films, pellets, shaped bodies, or monoliths) but provide important data for the evaluation and further selection of promising adsorbents for water harvesting from air. Accordingly, processing MOFs as shaped bodies may also change the kinetics of convective heat and mass transfer.

In devices relying on thermally induced desorption of water the thermal conductivity and heat capacity of the employed MOF are important. The specific heat capacities of MOFs are typically in the regime of 1 J g^{-1} K^{-1}, which is comparable to those of zeolites (e.g., zeolite 4A: $c_p = 0.915$ J g^{-1} K^{-1}) and equal approximately one quarter of that of water ($c_p = 4.19$ J g^{-1} K^{-1} at 15 °C and 101.325 kPa).[95] The relatively low heat capacity allows for short response times with respect to temperature changes and the linear temperature dependence of the heat capacity indicates the absence of thermal anomalies. Due to their open structures and the resulting low atomic number density, the thermal conductivity of MOFs is comparatively low. The imbalance between the long, flexible linkers and the heavy SBUs results in low phonon group velocities, suppressing the development of long range correlations and thereby reducing the mean free path of phonon modes.[96] The thermal conductivity of MOF-5 was shown to be governed by the short-range acoustic and the optical phonons, whereas the long-range acoustic phonons contribute only little to the total thermal conductivity.[96,97] Experimental studies show that MOF-5 has a thermal conductivity of 0.32 W m^{-1} K^{-1} (at 300 K); a rather low value for a crystalline material but in the same regime as that of zeolites (e.g., Zeolite 4A: $\kappa_{eff} = 0.16$–0.21 W m^{-1} K^{-1} at 300 K).[98] It should be noted, that the thermal conductivity is strongly dependent on the packing density.[99] Considering the necessity of shaped bodies or coatings when targeting large-scale applications, this limitation may be overcome by using additives with high thermal conductivity to make composite materials with tailored thermophysical properties.

5.3. Promising Materials and the Design of Next Generation MOFs for Water Harvesting From Air

The RH range in which adsorbents suitable for water harvesting from air ideally show a steep uptake strongly depends on the climate the device is expected to operate in. A steep uptake between 10% and 30% RH is generally desirable, since within this regime water is bound sufficiently strong but facile regeneration using low grade energy can still be achieved. Heat pumps for domestic heating are also preferably equipped with
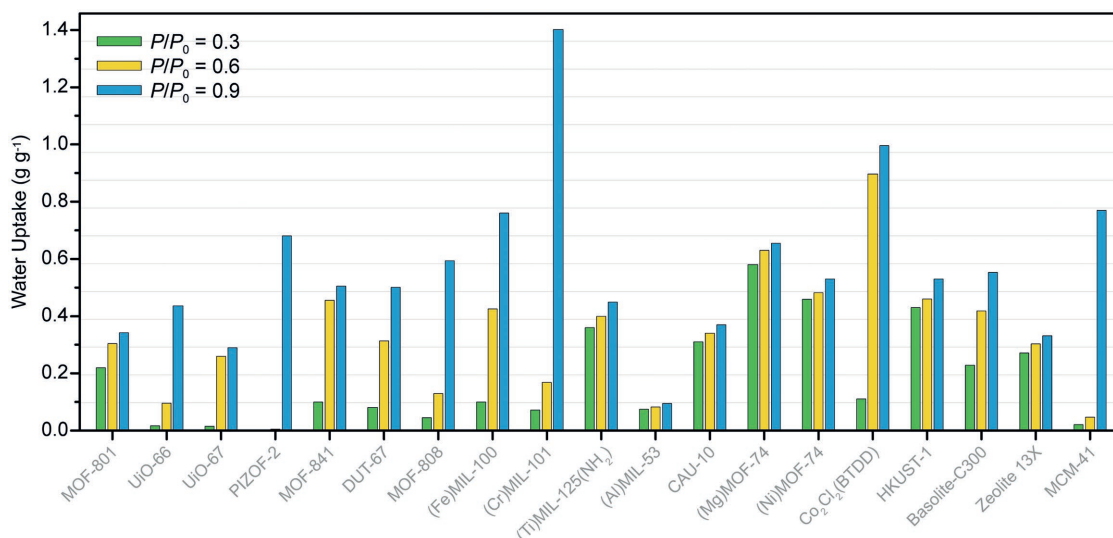
**ADVANCED
SCIENCE NEWS**

www.advancedsciencenews.com

**ADVANCED
MATERIALS**

www.advmat.de

Figure 18. Comparison of the water uptake of different porous materials at P/P_0 = 0.3, 0.6, and 0.9. A high water uptake at low relative pressures is desirable since it results in strong binding but also allows desorption under mild conditions.

adsorbents that adsorb water at comparatively low relative vapor pressure. MOFs for the application in adsorption-driven heat pumps have been extensively reviewed elsewhere and are out of the scope of this work.[62,63b,100] The actual vapor pressure range in which water uptake occurs therefore defines what application (i.e., water harvesting, heat pumps, or thermally driven chillers) and more precisely in the case of water harvesting, what climate the adsorbent is most suitable for.

The analysis of reported water adsorption isotherms, with respect to the inflection point, the capacity and the presence of hysteresis as well as the analysis of important structural features of the corresponding MOFs allows for the deduction of correlations, helpful in devising design principles for next generation materials. Such considerations have been reported for a series of MIL frameworks where the influence of appended functional groups capable of hydrogen bonding was studied.[59] In the following, a selection of structural parameters will be taken into consideration in order to establish design principles for MOFs suitable for the application in passive water harvesting devices. A compilation of MOFs with potential for the application in water-adsorption-based processes alongside selected structural parameters is given in **Table 2**.

5.3.1. Influence of the Linker Design

The exposed surface (van der Waals surface) and the polar surface of the organic linker can provide information on the hydrophilicity/hydrophobicity of the pores. Large, non-polar linkers (A_{vdW}/A_{polar} is large) result in hydrophobic pores, whereas small polar linkers (A_{vdW}/A_{polar} is small) generally render the pores hydrophilic. The hydrophilicity is however not directly linked to the polarity of a given organic molecule alone, but its determination is complex and in contrast to the polar surface, values cannot be calculated using simple computer software software.[65] As a rule of thumb, polar molecules capable of hydrogen bonding (acceptor/donor) are hydrophilic. One has to keep in mind that functionalities

such as nitro groups, esters, and ketones are considered hydroneutral and have no influence on the hydrophilicity of the linker. Linkers with large aromatic system like H₄BTEB used to prepare Y-**shp**-MOF-5 typically result in MOFs with water adsorption isotherms with inflection points located at high relative pressures whereas small and/or hydrophilic linkers such as the fumarate linker in MOF-801 or the FDC linker in MIL-160, respectively, render the pores hydrophilic, as indicated by low values of α. Introduction of heteroatoms capable of strong hydrogen bonding interactions allows for more hydrophilic pore environments leading to a shift of α to lower relative pressures. This is highlighted by theoretical isotherms calculated for a series of CAU-10 analogs (Figure 10) as well as the comparatively low value of α found for M_2Cl_2(BTDD) type compounds despite the large pore diameter (Figure 12).[11,69,73] The dimensionality of the pore structure appears to have little to no impact on the adsorption behavior as illustrated by the comparison of MOF-801 (4.8, 5.6, and 7.4 Å, 3D pore system, **fcu** topology) and CAU-10 (7 Å, 1D pore system, **yfm** topology), which both have similar pore volumes (V_p = 0.45 and 0.43 cm³ g⁻¹, respectively). The inflection point of both isotherms is located at low relative pressures (0.08 and 0.15, respectively) and the maximum capacities are identical (q_{max} = 0.36 g g⁻¹).[7,73] Comparison of isoreticular MOFs that only differ in the presence of a functionality allowing for efficient hydrogen bonding (e.g., −NH₂) reveal that such functionalization typically results in a lower value of α. The fact that these functionalities decrease the free pore volume however commonly leads to a concomitant decrease of the maximum capacity. Increasing the length of the linker affords a larger pore volume and a higher maximum capacity, but may be accompanied by a transition of the pores into the mesoporous regime, which typically results in a hysteresis between the adsorption and the desorption branch due to capillary condensation (D_C = 20.76 Å at 25 °C). It should however be noted that the critical diameter for capillary condensation under application conditions may differ from that at ambient conditions.

1704304 (21 of 26)

Table 2. Compilation of MOFs with interesting water adsorption properties (at 298 K). The capacity (q_{max}) and the inflection point (α) are related to structural features of the MOF. α is mainly governed by the hydrophilicity of the pore, the maximum capacity is correlated to the free pore volume (V_p) and the density (d_{cryst}). Hydrophilic functionalities as well as heteroaromatic linkers increasing the hydrophilicity of the pores shift α to lower relative pressures, whereas linkers with a large exposed nonpolar surface shift α toward high relative pressures.

	q_{max}[a] [g g⁻¹]	α	Pore size [Å]	V_p [cm³ g⁻¹]	d_{cryst} [g cm⁻³]	Linker, functionality	A_{vdW}, A_{polar}[b], HBD/A[c]	Topology pore structure	Ref.
MOF-801	0.28–0.36	0.08	4.8, 5.6, 7.4	0.27–0.45	1.68 (SC)	Fumarate, –	124.72, – no	**fcu**, 3D	[7]
UiO-66	0.44	0.36	7.4, 8.4	0.49	1.23	BDC, –	135.86, – np	**fcu**, 3D	[7,59,76b]
UiO-66(NH₂)	0.38	0.15	<Pristine	<Pristine	>Pristine	(NH₂)BDC, −NH₂	150.69, 26.02 yes	**fcu**, 3D	[59]
UiO-67	0.3	0.56	8.8, 16.6	0.99	1.04	BPDC, –	243.41, – no	**fcu**, 3D	[78]
UiO-67(NH₂)	0.26	0.2	<Pristine	0.64	>Pristine	(NH₂)BPDC, −NH₂	270.88, 52.04 yes	**fcu**, 3D	[78]
PIZOF-2	0.68	0.68	17.6	0.88	0.67	(OMe)₂PEDB, −(OMe)	593.86, 18.46 yes	**fcu-c**, 3D	[7]
MOF-841	0.51	0.26	9.2	0.53	1.05	MTB, –	485.36, – no	**flu**, 3D	[7]
DUT-67	0.5	0.37	11.7, 14.2	0.6	1.06	TDC, thiophene	115.36, 28.24 yes	**reo**, 3D	[7]
DUT-51	0.54	0.64	15.6, 18.8	1.08	1.44	DTTDC, thipophene	199.73, 84.73 yes	**reo**, 3D	[25b,31b]
MOF-808	0.59	0.33	18.4	0.84	0.86	BTC, –	135.86, – no	**spn**, 3D	[7]
(Al)MIL-100	0.5	0.32	25, 39	1.14	0.80	BTC, –	135.86, – no	**mtn**, 3D	[58]
(Cr)MIL-101	1.4	0.46	29, 34	1.68	0.61	BDC, –	135.86, – no	**mtn**, 3D	[59]
(Cr)MIL-101(NH₂)	0.82	0.38	<Pristine	<Pristine	>Pristine	(NH₂)BDC, −NH₂	150.69, 26.02 yes	**mtn**, 3D	[59,64]
(Ti)MIL-125(NH₂)	0.67	0.23	5.1, 12.5	0.7	0.76	(NH₂)BDC, −NH₂	150.69, 26.02 yes	**bcu**, 3D	[59]
BASF A-520	0.42	0.28	6	0.47	1.06	Fumarate, –	124.72, – no	**sra**, 1D	[7,101]
(Al)MIL-53	0.09	0.24	7–13	0.51	n.d.	BDC, –	135.86, – no	**sra**, 1D	[59]
CAU-1	0.55	0.38	5, 10	0.55	0.88	(NH₂)BDC, −NH₂	150.69, 26.02 yes	**bcu**, 3D	[102]
CAU-1(NHCH₃)	0.40	0.48	<Pristine	0.40	>Pristine	(NHCH₃)BDC, −(NHCH₃)	187.52, 12.03 yes	**bcu**, 3D	[102a]
CAU-1(NHCOCH₃)	0.25	0.36	<Pristine	0.30	>Pristine	(NHCOCH₃)BDC, −(NHCOCH₃)	211.77, 29.10 yes	**bcu**, 3D	[102a]
CAU-10(H)	0.36	0.15-0.25	7	0.43	1.37	m-BDC, –	135.86, – no	**yfm**, 1D	[103]
CAU-10(CH₃)	0.23	0.45	<Pristine	–	>Pristine	m-(CH₃)BDC, −(CH₃)	168.11, – no	**yfm**, 1D	[69b]
CAU-10(NH₂)	0.24	0.11	<Pristine	–	>Pristine	m-(NH₂)BDC, −NH₂	150.69, 26.02 yes	**yfm**, 1D	[69b]
CAU-10(OCH₃)	0.08	0.25	<Pristine	–	>Pristine	m-(OCH₃)BDC, −(OCH₃)	183.99, 9.23 yes	**yfm**, 1D	[69b]
CAU-10(NO₂)	0.33	0.17	<Pristine	0.21	>Pristine	m-(NO₂)BDC, −(NO₂)	176.67, 45.82 no	**yfm**, 1D	[69b]
MIL-160	0.38	0.10	5	0.48	N.A.	FDC, furan	108.06, 13.14 yes	**yfm**, 1D	[72]
Co₂Cl₂(BTDD)	0.97	0.29	17	0.90	0.70	(BTDD), dioxine	156.77, 18.46 yes	**etb**, 1 D	[11]
Y-shp-MOF-5	0.5	0.64	12	0.63	0.97	BTEB, –	564.05, – no	**shp**, 1D	[56b]
(Mg)MOF-74	0.54	0.05	11.1	0.53	0.91	DOT, OMS	135.86, – no	**etb**, 1D	[34c]

[a]Determined a $P/P_0 = 0.9$; [b]HBD/A: hydrogen bond donor/acceptor; [c]A_{vdW}: van der Waals surface area of the linker; A_{polar}: polar surface area of the linker. Values were calculated using MarvinSketch.[24] Binding groups were considered part of the SBU.

Typically, desorption in passive water harvesting devices is achieved by increasing the temperature (TSA) resulting in an increased critical diameter for capillary condensation (see Equation (1)). A hysteretic behavior can also be observed when water superclusters are formed, since breaking up the comparably strong hydrogen bonds requires a significant decrease of the partial pressure, such behavior was reported for Y-**shp**-MOF-5.[56b] Noncapillary condensation hysteresis loops may also be observed for microporous flexible frameworks.[59] As illustrated by the dramatically different water sorption of a series of isoreticular functionalized MIL-53 frameworks, it is not possible to predict the occurrence of a breathing or gate opening motion (Figure 14).

5.3.2. Influence of the SBU

The use of heavy, highly charged metal ions such as zirconium yields MOFs with high stability in the presence of water due to strong bonding. However, their high atomic weight negatively influences the gravimetric uptake. Therefore, the use of lighter elements such as aluminum, titanium, or iron is favorable in achieving a high gravimetric uptake. It has been shown, that bridging −OH groups within the SBUs can act as primary adsorption sites.[7,72] Such sites are frequently found in Zr_6O_8 based and many rod-like SBUs. Apart from the physical properties and the structural diversity arising from the use of certain metals for the construction of MOFs, their toxicology has to be

considered, as partial dissolution of the MOF can result in contamination of the harvested water. In general, the use of both, linkers and metals with a low LD_{50} such as H_2BDC or H_3BTC and Al, Ti, or Fe is preferable for the construction of MOFs for water harvesting applications.[104]

5.3.3. The Influence of Defects

The presence of defects on the gas adsorption behavior of MOFs has been intensively studied especially in zirconium MOFs having an **fcu** topology such as UiO-66.[105] However, only few reports discussing the impact of defects on water adsorption have been reported.[7,105a,d] The isotherms of single crystal and powder samples of MOF-801 show different inflection points and adsorption capacities. This was ascribed to the presence of defects in the powder sample rendering the pores more hydrophilic and increasing the pore volume, thereby shifting the inflection point to lower relative pressures and increasing the maximum capacity.[7] Studies of the influence of defects in the structure of UiO-66 on its water adsorption isotherm confirm these findings.[105d] Interestingly, experimental BET surface areas determined by nitrogen sorption are relatively insensitive toward the presence of defects, whereas water adsorption isotherms show significant changes depending on the concentration of defects. This is supported by Q_{st} values of water adsorption calculated for ideal (defect free) UiO-66 and UiO-66 with two different concentrations of defects. The hydrophobic nature of ideal UiO-66 results in low initial Q_{st} values (-15 kJ mol^{-1}) that sharply increase at higher loading, plateauing at -60 kJ mol^{-1}. In contrast, heats of adsorption of UiO-66 containing defects show high initial Q_{st} values (-60 to -70 kJ mol^{-1}) that gradually decrease at higher loadings, indicative of hydrophilic pores. The combination of nitrogen, argon, and water adsorption isotherms has been suggested for the detailed characterization of classical porous materials, since water adsorption, including the capacity, pore filling pressure (inflection point), and hysteresis behavior, are sensitive to subtle changes in size, geometry, and surface chemistry of the pore system.[106]

6. Conclusion

We have highlighted recent developments in the chemistry of metal–organic frameworks with respect to their utilization for water harvesting from air. With regard to their stability, a thorough understanding of the degradation pathways and subsequent adaptation of materials has afforded MOFs with exceptional hydrolytic stability. Recently, it was demonstrated that harvesting water from air using MOFs in a device driven by low-grade energy is indeed feasible. This proof-of-concept device can operate under low relative humidity conditions, which lends credence to the notion that this idea can eventually address the great challenge of providing drinking water to arid regions using off-grid energy sources such as sunlight. At this point the challenge is three-fold. First, selection of MOFs with improved working capacities under temperature and/or pressure swing conditions is necessary to optimize the inherent performance of the adsorbents. Second, it is crucial to derive

a more detailed understanding of the sorption kinetics which, at this point, is still lacking. A detailed understanding of the adsorption mechanism of water in MOFs of diverse structure types with different pore shapes and metrics provides the basis for the deduction of design principles for next generation MOFs with promising performance for the application in water harvesting devices. Third, while the performance of MOF adsorbents is highly promising, a lot remains to be done with respect to device-engineering to render this technology viable for supplying fresh water to regions experiencing water stress.

Conflict of Interest

The authors declare no conflict of interest.

[1] L. Pfister, H. H. Savenije, F. Fenicia, *Leonardo Da Vinci's Water Theory: On the Origin and Fate of Water*, International Association of Hydrological Science (IAHS) Special Publication 9, Oxfordshire, UK **2009**.

[2] P. H. Gleick, *Water in Crisis: A Guide to the Worlds Fresh Water Resources*, Oxford University Press, New York **1993**.

[3] C. J. Vörösmarty, P. Green, J. Salisbury, R. B. Lammers, *Science* **2000**, *289*, 284.

[4] B. Van der Bruggen, C. Vandecasteele, *Desalination* **2002**, *143*, 207.

[5] a) R. S. Schemenauer, P. Cereceda, *J. Appl. Meteorol.* **1994**, *33*, 1313; b) O. Klemm, R. S. Schemenauer, A. Lummerich, P. Cereceda, V. Marzol, D. Corell, J. van Heerden, D. Reinhard, T. Gherezghiher, J. Olivier, P. Osses, J. Sarsour, E. Frost, M. J. Estrela, J. A. Valiente, G. M. Fessehaye, *Ambio* **2012**, *41*, 221; c) K.-C. Park, S. S. Chhatre, S. Srinivasan, R. E. Cohen, G. H. McKinley, *Langmuir* **2013**, *29*, 13269; d) R. V. Wahlgren, *Water Res.* **2001**, *35*, 1; e) M. Muselli, D. Beysens, J. Marcillat, I. Milimouk, T. Nilsson, A. Louche, *Atmos. Res.* **2002**, *64*, 297; f) O. Clus, P. Ortega, M. Muselli, I. Milimouk, D. Beysens, *J. Hydrol.* **2008**, *361*, 159; g) A. Lee, M.-W. Moon, H. Lim, W.-D. Kim, H.-Y. Kim, *Langmuir* **2012**, *28*, 10183; h) G. E. William, M. Mohamed, M. Fatouh, *Energy* **2015**, *90*, 1707.

[6] G. Restuccia, A. Freni, S. Vasta, Y. Aristov, *Int. J. Refrig.* **2004**, *27*, 284.

[7] H. Furukawa, F. Gándara, Y.-B. Zhang, J. Jiang, W. L. Queen, M. R. Hudson, O. M. Yaghi, *J. Am. Chem. Soc.* **2014**, *136*, 4369.

[8] A. J. Howarth, Y. Liu, P. Li, Z. Li, T. C. Wang, J. T. Hupp, O. K. Farha, *Nat. Rev. Mater.* **2016**, *1*, 15018.

[9] N. C. Burtch, H. Jasuja, K. S. Walton, *Chem. Rev.* **2014**, *114*, 10575.

[10] a) E. J. Carrington, C. A. McAnally, A. J. Fletcher, S. P. Thompson, M. Warren, L. Brammer, *Nat. Chem.* **2017**; b) C. Serre, F. Millange, C. Thouvenot, M. Noguès, G. Marsolier, D. Louër, G. Férey, *J. Am. Chem. Soc.* **2002**, *124*, 13519.

[11] A. J. Rieth, S. Yang, E. N. Wang, M. Dinc, *ACS Cent. Sci.* **2017**, *3*, 668.

[12] J. B. DeCoste, G. W. Peterson, B. J. Schindler, K. L. Killops, M. A. Browe, J. J. Mahle, *J. Mater. Chem. A* **2013**, *1*, 11922.

[13] K. Tan, S. Zuluaga, Q. Gong, P. Canepa, H. Wang, J. Li, Y. J. Chabal, T. Thonhauser, *Chem. Mater.* **2014**, *26*, 6886.

[14] M. P. Singh, N. R. Dhumal, H. J. Kim, J. Kiefer, J. A. Anderson, *J. Phys. Chem. C* **2016**, *120*, 17323.

[15] P. Guo, D. Dutta, A. G. Wong-Foy, D. W. Gidley, A. J. Matzger, *J. Am. Chem. Soc.* **2015**, *137*, 2651.

[16] a) M. Haouas, C. Martineau, F. Taulelle, in *eMagRes*, John Wiley & Sons, Ltd, Chichester, UK **2007**; b) R. W. Flaig, T. M. Osborn Popp, A. M. Fracaroli, E. A. Kapustin, M. J. Kalmutzki, R. M. Altamimi, F. Fathieh, J. A. Reimer, O. M. Yaghi, *J. Am. Chem. Soc.* **2017**, *139*, 12125.

[17] a) D. Kolokolov, A. Stepanov, V. Guillerm, C. Serre, B. Frick, H. Jobic, *J. Phys. Chem. C* **2012**, *116*, 12131; b) D. I. Kolokolov, H. Jobic, A. G. Stepanov, V. Guillerm, T. Devic, C. Serre, G. Férey, *Angew. Chem.* **2010**, *122*, 4901.

[18] F. Gul-E-Noor, B. Jee, A. Pöppl, M. Hartmann, D. Himsl, M. Bertmer, *Phys. Chem. Chem. Phys.* **2011**, *13*, 7783.

[19] J. J. Low, A. I. Benin, P. Jakubczak, J. F. Abrahamian, S. A. Faheem, R. R. Willis, *J. Am. Chem. Soc.* **2009**, *131*, 15834.

[20] J. B. DeCoste, G. W. Peterson, H. Jasuja, T. G. Glover, Y.-G. Huang, K. S. Walton, *J. Mater. Chem. A* **2013**, *1*, 5642.

[21] P. Küsgens, M. Rose, I. Senkovska, H. Fröde, A. Henschel, S. Siegle, S. Kaskel, *Microporous Mesoporous Mater.* **2009**, *120*, 325.

[22] M. De Toni, R. Jonchiere, P. Pullumbi, F. X. Coudert, A. H. Fuchs, *ChemPhysChem* **2012**, *13*, 3497.

[23] a) H. J. Choi, M. Dinc, A. Dailly, J. R. Long, *Energy Environ. Sci.* **2010**, *3*, 117; b) V. Colombo, S. Galli, H. J. Choi, G. D. Han, A. Maspero, G. Palmisano, N. Masciocchi, J. R. Long, *Chem. Sci.* **2011**, *2*, 1311.

[24] ChemAxon, http://www.chemaxon.com/ **2017**, (accessed: June 2017).

[25] a) J. H. Cavka, S. Jakobsen, U. Olsbye, N. Guillou, C. Lamberti, S. Bordiga, K. P. Lillerud, *J. Am. Chem. Soc.* **2008**, *130*, 13850; b) V. Bon, I. Senkovska, I. A. Baburin, S. Kaskel, *Cryst. Growth Des.* **2013**, *13*, 1231.

[26] P. Li, N. A. Vermeulen, X. Gong, C. D. Malliakas, J. F. Stoddart, J. T. Hupp, O. K. Farha, *Angew. Chem.* **2016**, *128*, 10514.

[27] a) J. Liu, A. I. Benin, A. M. Furtado, P. Jakubczak, R. R. Willis, M. D. LeVan, *Langmuir* **2011**, *27*, 11451; b) A. C. Kizzie, A. G. Wong-Foy, A. J. Matzger, *Langmuir* **2011**, *27*, 6368.

[28] a) F. Jeremias, V. Lozan, S. K. Henninger, C. Janiak, *Dalton Trans.* **2013**, *42*, 15967; b) X. Liu, N. K. Demir, Z. Wu, K. Li, *J. Am. Chem. Soc.* **2015**, *137*, 6999.

[29] J. E. Mondloch, M. J. Katz, N. Planas, D. Semrouni, L. Gagliardi, J. T. Hupp, O. K. Farha, *Chem. Commun.* **2014**, *50*, 8944.

[30] S. Øien-Ødegaard, B. Bouchevreau, K. Hylland, L. Wu, R. Blom, C. Grande, U. Olsbye, M. Tilset, K. P. Lillerud, *Inorg. Chem.* **2016**, *55*, 1986.

[31] a) V. Guillerm, F. Ragon, M. Dan-Hardi, T. Devic, M. Vishnuvarthan, B. Campo, A. Vimont, G. Clet, Q. Yang, G. Maurin, *Angew. Chem., Int. Ed.* **2012**, *51*, 9267; b) V. Bon, V. Senkovskyy, I. Senkovska, S. Kaskel, *Chem. Commun.* **2012**, *48*,

8407; c) H.-L. Jiang, D. Feng, K. Wang, Z.-Y. Gu, Z. Wei, Y.-P. Chen, H.-C. Zhou, *J. Am. Chem. Soc.* **2013**, *135*, 13934.

[32] a) D. Ma, Y. Li, Z. Li, *Chem. Commun.* **2011**, *47*, 7377; b) T. A. Makal, X. Wang, H.-C. Zhou, *Cryst. Growth Des.* **2013**, *13*, 4760.

[33] L. Liu, S. G. Telfer, *J. Am. Chem. Soc.* **2015**, *137*, 3901.

[34] a) D. N. Dybtsev, H. Chun, K. Kim, *Angew. Chem.* **2004**, *116*, 5143; b) N. C. Burtch, K. S. Walton, *Acc. Chem. Res.* **2015**, *48*, 2850; c) P. M. Schoenecker, C. G. Carson, H. Jasuja, C. J. Flemming, K. S. Walton, *Ind. Eng. Chem. Res.* **2012**, *51*, 6513.

[35] H. Jasuja, N. C. Burtch, Y.-G. Huang, Y. Cai, K. S. Walton, *Langmuir* **2013**, *29*, 633.

[36] a) S. S. Kaye, A. Dailly, O. M. Yaghi, J. R. Long, *J. Am. Chem. Soc.* **2007**, *129*, 14176; b) T. Wu, L. Shen, M. Luebbers, C. Hu, Q. Chen, Z. Ni, R. I. Masel, *Chem. Commun.* **2010**, *46*, 6120; c) J. Yang, A. Grzech, F. M. Mulder, T. J. Dingemans, *Chem. Commun.* **2011**, *47*, 5244.

[37] L. Bellarosa, J. J. Gutiérrez-Sevillano, S. Calero, N. López, *Phys. Chem. Chem. Phys.* **2013**, *15*, 17696.

[38] a) H. Jasuja, K. S. Walton, *Dalton Trans.* **2013**, *42*, 15421; b) J. Park, J.-R. Li, Y.-P. Chen, J. Yu, A. A. Yakovenko, Z. U. Wang, L.-B. Sun, P. B. Balbuena, H.-C. Zhou, *Chem. Commun.* **2012**, *48*, 9995.

[39] G. Férey, C. Mellot-Draznieks, C. Serre, F. Millange, J. Dutour, S. Surblé, I. Margiolaki, *Science* **2005**, *309*, 2040.

[40] a) Y. Zang, J. Shi, X. Zhao, L. Kong, F. Zhang, Y. Zhong, *React. Kinet., Mech. Catal.* **2013**, *109*, 77; b) J. Juan-Alcañiz, E. V. Ramos-Fernandez, U. Lafont, J. Gascon, F. Kapteijn, *J. Catal.* **2010**, *269*, 229.

[41] I. J. Kang, N. A. Khan, E. Haque, S. H. Jhung, *Chem. Eur. J.* **2011**, *17*, 6437.

[42] a) T.-H. Chen, I. Popov, O. Zenasni, O. Daugulis, O. Š. Miljani, *Chem. Commun.* **2013**, *49*, 6846; b) N. Nijem, P. Canepa, U. Kaipa, K. Tan, K. Roodenko, S. Tekarli, J. Halbert, I. W. H. Oswald, R. K. Arvapally, C. Yang, T. Thonhauser, M. A. Omary, Y. J. Chabal, *J. Am. Chem. Soc.* **2013**, *135*, 12615; c) T. Li, D.-L. Chen, J. E. Sullivan, M. T. Kozlowski, J. K. Johnson, N. L. Rosi, *Chem. Sci.* **2013**, *4*, 1746.

[43] J. G. Nguyen, S. M. Cohen, *J. Am. Chem. Soc.* **2010**, *132*, 4560.

[44] T. K. Pal, D. De, S. Senthilkumar, S. Neogi, P. K. Bharadwaj, *Inorg. Chem.* **2016**, *55*, 7835.

[45] a) C. Yang, U. Kaipa, Q. Z. Mather, X. Wang, V. Nesterov, A. F. Venero, M. A. Omary, *J. Am. Chem. Soc.* **2011**, *133*, 18094; b) C. Serre, *Angew. Chem., Int. Ed.* **2012**, *51*, 6048.

[46] a) A. Comotti, S. Bracco, P. Sozzani, S. Horike, R. Matsuda, J. Chen, M. Takata, Y. Kubota, S. Kitagawa, *J. Am. Chem. Soc.* **2008**, *130*, 13664; b) S. Paranthaman, F.-X. Coudert, A. H. Fuchs, *Phys. Chem. Chem. Phys.* **2010**, *12*, 8124.

[47] J. Cousin Saint Remi, T. Rémy, V. Van Hunskerken, S. van de Perre, T. Duerinck, M. Maes, D. De Vos, E. Gobechiya, C. E. Kirschhock, G. V. Baron, *ChemSusChem* **2011**, *4*, 1074.

[48] a) R. P. Lively, M. E. Dose, J. A. Thompson, B. A. McCool, R. R. Chance, W. J. Koros, *Chem. Commun.* **2011**, *47*, 8667; b) A. U. Ortiz, A. P. Freitas, A. Boutin, A. H. Fuchs, F.-X. Coudert, *Phys. Chem. Chem. Phys.* **2014**, *16*, 9940.

[49] a) F.-K. Shieh, S.-C. Wang, S.-Y. Leo, K. C. W. Wu, *Chem. Eur. J.* **2013**, *19*, 11139; b) K. Zhang, R. P. Lively, M. E. Dose, A. J. Brown, C. Zhang, J. Chung, S. Nair, W. J. Koros, R. R. Chance, *Chem. Commun.* **2013**, *49*, 3245.

[50] a) S. S.-Y. Chui, S. M.-F. Lo, J. P. H. Charmant, A. G. Orpen, I. D. Williams, *Science* **1999**, *283*, 1148; b) Y. He, B. Chen, *Encyclopedia of Inorganic and Bioinorganic Chemistry*, Wiley Online Library, **2014**; c) N. L. Rosi, J. Kim, M. Eddaoudi, B. Chen, M. O'Keeffe, O. M. Yaghi, *J. Am. Chem. Soc.* **2005**, *127*, 1504.

[51] W. S. Drisdell, R. Poloni, T. M. McDonald, J. R. Long, B. Smit, J. B. Neaton, D. Prendergast, J. B. Kortright, *J. Am. Chem. Soc.* **2013**, *135*, 18183.

[52] P. D. Dietzel, R. E. Johnsen, R. Blom, H. Fjellvåg, *Chem. Eur. J.* **2008**, *14*, 2389.

[53] a) L. Valenzano, B. Civalleri, S. Chavan, S. Bordiga, M. H. Nilsen, S. Jakobsen, K. P. Lillerud, C. Lamberti, *Chem. Mater.* **2011**, *23*, 1700; b) A. D. Wiersum, E. Soubeyrand-Lenoir, Q. Yang, B. Moulin, V. Guillerm, M. B. Yahia, S. Bourrelly, A. Vimont, S. Miller, C. Vagner, *Chem. Asian J.* **2011**, *6*, 3270.

[54] G. Wißmann, A. Schaate, S. Lilienthal, I. Bremer, A. M. Schneider, P. Behrens, *Microporous Mesoporous Mater.* **2012**, *152*, 64.

[55] a) J. K. Brennan, T. J. Bandosz, K. T. Thomson, K. E. Gubbins, *Colloids Surf., A* **2001**, *187*, 539; b) K. Kaneko, Y. Hanzawa, T. Iiyama, T. Kanda, T. Suzuki, *Adsorption* **1999**, *5*, 7.

[56] a) F. o.-X. Coudert, A. Boutin, A. H. Fuchs, A. V. Neimark, *J. Phys. Chem. Lett.* **2013**, *4*, 3198; b) R. G. AbdulHalim, P. M. Bhatt, Y. Belmabkhout, A. Shkurenko, K. Adil, L. J. Barbour, M. Eddaoudi, *J. Am. Chem. Soc.* **2017**, *139*, 10715.

[57] G. Akiyama, R. Matsuda, H. Sato, A. Hori, M. Takata, S. Kitagawa, *Microporous Mesoporous Mater.* **2012**, *157*, 89.

[58] F. Jeremias, A. Khutia, S. K. Henninger, C. Janiak, *J. Mater. Chem.* **2012**, *22*, 10148.

[59] J. Canivet, J. Bonnefoy, C. Daniel, A. Legrand, B. Coasne, D. Farrusseng, *New J. Chem.* **2014**, *38*, 3102.

[60] G. Férey, C. Mellot-Draznieks, C. Serre, F. Millange, *Acc. Chem. Res.* **2005**, *38*, 217.

[61] a) C. Janiak, S. K. Henninger, *Chimia* **2013**, *67*, 419; b) S. K. Henninger, F. Jeremias, H. Kummer, C. Janiak, *Eur. J. Inorg. Chem.* **2012**, *2012*, 2625; c) J. Ehrenmann, S. K. Henninger, C. Janiak, *Eur. J. Inorg. Chem.* **2011**, *2011*, 471; d) G. Akiyama, R. Matsuda, S. Kitagawa, *Chem. Lett.* **2010**, *39*, 360.

[62] J. Canivet, A. Fateeva, Y. Guo, B. Coasne, D. Farrusseng, *Chem. Soc. Rev.* **2014**, *43*, 5594.

[63] a) E. Elsayed, A.-D. Raya, S. Mahmoud, P. A. Anderson, A. Elsayed, P. G. Youssef, *Desalination* **2017**, *406*, 25; b) M. F. de Lange, K. J. Verouden, T. J. Vlugt, J. Gascon, F. Kapteijn, *Chem. Rev.* **2015**, *115*, 12205.

[64] N. Ko, P. G. Choi, J. Hong, M. Yeo, S. Sung, K. E. Cordova, H. J. Park, J. K. Yang, J. Kim, *J. Mater. Chem. A* **2015**, *3*, 2057.

[65] a) V. Gutmann, *Electrochim. Acta* **1976**, *21*, 661; b) V. Gutmann, *The Donor-Acceptor Approach to Molecular Interactions*, Plenum Press, New York **1978**; c) N. Sagawa, T. Shikata, *Phys. Chem. Chem. Phys.* **2014**, *16*, 13262.

[66] A. Khutia, H. U. Rammelberg, T. Schmidt, S. Henninger, C. Janiak, *Chem. Mater.* **2013**, *25*, 790.

[67] J. Liu, Y. Wang, A. I. Benin, P. Jakubczak, R. R. Willis, M. D. LeVan, *Langmuir* **2010**, *26*, 14301.

[68] Y. Kuwahara, T. Ohmichi, T. Kamegawa, K. Mori, H. Yamashita, *J. Mater. Chem.* **2010**, *20*, 5052.

[69] a) D. Fröhlich, S. K. Henninger, C. Janiak, *Dalton Trans.* **2014**, *43*, 15300; b) H. Reinsch, M. A. van der Veen, B. Gil, B. Marszalek, T. Verbiest, D. De Vos, N. Stock, *Chem. Mater.* **2012**, *25*, 17.

[70] D. Fröhlich, E. Pantatosaki, P. D. Kolokathis, K. Markey, H. Reinsch, M. Baumgartner, M. A. van der Veen, D. E. De Vos, N. Stock, G. K. Papadopoulos, *J. Mater. Chem. A* **2016**, *4*, 11859.

[71] H. Reinsch, S. Waitschat, N. Stock, *Dalton Trans.* **2013**, *42*, 4840.

[72] A. Cadiau, J. S. Lee, D. Damasceno Borges, P. Fabry, T. Devic, M. T. Wharmby, C. Martineau, D. Foucher, F. Taulelle, C. H. Jun, *Adv. Mater.* **2015**, *27*, 4775.

[73] D. D. Borges, G. Maurin, D. S. Galvão, *MRS Adv.* **2017**, *2*, 519.

[74] a) S. K. Henninger, H. A. Habib, C. Janiak, *J. Am. Chem. Soc.* **2009**, *131*, 2776; b) C. Janiak, S. K. Henninger, *Nachr. Chem.* **2013**, *61*, 520.

[75] H. Kim, S. Yang, S. R. Rao, S. Narayanan, E. A. Kapustin, H. Furukawa, A. S. Umans, O. M. Yaghi, E. N. Wang, *Science* **2017**, *356*, 430.

[76] a) E. Soubeyrand-Lenoir, C. Vagner, J. W. Yoon, P. Bazin, F. Ragon, Y. K. Hwang, C. Serre, J.-S. Chang, P. L. Llewellyn, *J. Am. Chem. Soc.* **2012**, *134*, 10174; b) G. E. Cmarik, M. Kim, S. M. Cohen, K. S. Walton, *Langmuir* **2012**, *28*, 15606.

[77] a) H. Jasuja, J. Zang, D. S. Sholl, K. S. Walton, *J. Phys. Chem. C* **2012**, *116*, 23526; b) H. Jasuja, K. S. Walton, *J. Phys. Chem. C* **2013**, *117*, 7062.

[78] N. Ko, J. Hong, S. Sung, K. E. Cordova, H. J. Park, J. K. Yang, J. Kim, *Dalton Trans.* **2015**, *44*, 2047.

[79] D. Do, S. Junpirom, H. Do, *Carbon* **2009**, *47*, 1466.

[80] a) C. Triguero, F.-X. Coudert, A. Boutin, A. H. Fuchs, A. V. Neimark, *J. Chem. Phys.* **2012**, *137*, 184702; b) G. Férey, C. Serre, *Chem. Soc. Rev.* **2009**, *38*, 1380; c) K. Uemura, R. Matsuda, S. Kitagawa, *J. Solid State Chem.* **2005**, *178*, 2420; d) H. Depauw, I. Nevjestic, K. Leus, G. Wang, F. Callens, H. Vrielinck, P. Van Der Voort, presented at *5th Int. Conf. on Metal-Organic Frameworks & Open Framework Compounds (MOF 2016)*, **2016**; e) J. Arınez-Soriano, J. Albalad, C. Vila-Parrondo, J. Pérez-Carvajal, S. Rodrıguez-Hermida, A. Cabeza, J. Juanhuix, I. Imaz, D. Maspoch, *Chem. Commun* **2016**, *52*, 7229.

[81] F. Millange, C. Serre, G. Ferey, *Chem. Commun.* **2002**, 822.

[82] A. Boutin, F.-X. Coudert, M.-A. Springuel-Huet, A. V. Neimark, G. Férey, A. H. Fuchs, *J. Phys. Chem. C* **2010**, *114*, 22237.

[83] S. Devautour-Vinot, G. Maurin, F. Henn, C. Serre, G. Férey, *Phys. Chem. Chem. Phys.* **2010**, *12*, 12478.

[84] F.-X. Coudert, A. U. Ortiz, V. Haigis, D. Bousquet, A. H. Fuchs, A. Ballandras, G. Weber, I. Bezverkhyy, N. Geoffroy, J.-P. Bellat, *J. Phys. Chem. C* **2014**, *118*, 5397.

[85] A. Shigematsu, T. Yamada, H. Kitagawa, *J. Am. Chem. Soc.* **2011**, *133*, 2034.

[86] a) T. Lescouet, E. Kockrick, G. Bergeret, M. Pera-Titus, S. Aguado, D. Farrusseng, *J. Mater. Chem.* **2012**, *22*, 10287; b) T. Lescouet, E. Kockrick, G. Bergeret, M. Pera-Titus, D. Farrusseng, *Dalton Trans.* **2011**, *40*, 11359.

[87] T. Loiseau, C. Serre, C. Huguenard, G. Fink, F. Taulelle, M. Henry, T. Bataille, G. Férey, *Chem. Eur. J.* **2004**, *10*, 1373.

[88] a) M. Wickenheisser, A. Herbst, R. Tannert, B. Milow, C. Janiak, *Microporous Mesoporous Mater.* **2015**, *215*, 143; b) M. Wickenheisser, T. Paul, C. Janiak, *Microporous Mesoporous Mater.* **2016**, *220*, 258; c) N. U. Qadir, S. A. Said, R. B. Mansour, K. Mezghani, A. Ul-Hamid, *Dalton Trans.* **2016**, *45*, 15621; d) E. Elsayed, H. Wang, P. A. Anderson, R. Al-Dadah, S. Mahmoud, H. Navarro, Y. Ding, J. Bowen, *Microporous Mesoporous Mater.* **2017**, *244*, 180; e) K. Uma, G.-T. Pan, T. C.-K. Yang, *Materials* **2017**, *10*, 610.

[89] a) M. Gaab, N. Trukhan, S. Maurer, R. Gummaraju, U. Müller, *Microporous Mesoporous Mater.* **2012**, *157*, 131; b) H. Kummer, F. Jeremias, A. Warlo, G. Füldner, D. Fröhlich, C. Janiak, R. Gläser, S. K. Henninger, *Ind. Eng. Chem. Res.* **2017**, *56*, 8393.

[90] a) A. Permyakova, S. Wang, E. Courbon, F. Nouar, N. Heymans, P. D'Ans, N. Barrier, P. Billemont, G. De Weireld, N. Steunou, M. Frere, C. Serre, *J. Mater. Chem. A* **2017**, *5*, 12889; b) L. Garzón-Tovar, J. Pérez-Carvajal, I. Imaz, D. Maspoch, *Adv. Funct. Mater.* **2017**, *27*, 1606424.

[91] F. Jeremias, D. Frohlich, C. Janiak, S. K. Henninger, *New J. Chem.* **2014**, *38*, 1846.

[92] a) C. Perego, P. Villa, *Catal. Today* **1997**, *34*, 281; b) M. Hesse, U. Mueller, O. Yaghi, (Google), Patents, **2009**; c) A. Czaja, E. Leung, N. Trukhan, U. Müller, *Metal-Organic Frameworks*, Wiley-VCH, Weinheim **2011**, p. 337.

[93] a) N. Stock, S. Biswas, *Chem. Rev.* **2012**, *112*, 933; b) Q.-L. Zhu, Q. Xu, *Chem. Soc. Rev.* **2014**, *43*, 5468; c) J.-R. Li, J. Sculley, H.-C. Zhou, *Chem. Rev.* **2012**, *112*, 869; d) S. Qiu, M. Xue, G. Zhu, *Chem. Soc. Rev.* **2014**, *43*, 6116.

[94] a) H. W. B. Teo, A. Chakraborty, S. Kayal, *Appl. Therm. Eng.* **2017**, *120*, 453; b) H. W. B. Teo, A. Chakraborty, Y. Kitagawa, S. Kayal, *Int. J. Heat Mass Transfer* **2017**, *114*, 621; c) E. Alvarez, N. Guillou, C. Martineau, B. Bueken, B. Van de Voorde, C. Le Guillouzer,

P. Fabry, F. Nouar, F. Taulelle, D. de Vos, J.-S. Chang, K. H. Cho, N. Ramsahye, T. Devic, M. Daturi, G. Maurin, C. Serre, *Angew. Chem., Int. Ed.* **2015**, *54*, 3664.

[95] a) F. A. Kloutse, R. Zacharia, D. Cossement, R. Chahine, *Microporous Mesoporous Mater.* **2015**, *217*, 1; b) B. Mu, K. S. Walton, *J. Phys. Chem. C* **2011**, *115*, 22748; c) L. Qiu, V. Murashov, M. A. White, *Solid State Sci.* **2000**, *2*, 841.

[96] B. L. Huang, A. J. H. McGaughey, M. Kaviany, *Int. J. Heat Mass Trans.* **2007**, *50*, 393.

[97] L. Han, M. Budge, P. Alex Greaney, *Comput. Mater. Sci.* **2014**, *94*, 292.

[98] a) B. L. Huang, Z. Ni, A. Millward, A. J. H. McGaughey, C. Uher, M. Kaviany, O. Yaghi, *Int. J. Heat Mass Transfer* **2007**, *50*, 405; b) A. McGaughey, M. Kaviany, *Int. J. Heat Mass Transfer* **2004**, *47*, 1799; c) B. Dawoud, M. I. Sohel, A. Freni, S. Vasta, G. Restuccia, *Appl. Therm. Eng.* **2011**, *31*, 2241.

[99] M. Khaliji Oskouei, Z. Tamainot-Telto, presented at *Proc. of the 10th Int. Conf. on Heat Transfer, Fluid Mechanics and Mechanics and Thermodynamics (HEFAT2014)*, **2014**.

[100] N. C. Burtch, H. Jasuja, K. S. Walton, *Chem. Rev* **2014**, *114*, 10575.

[101] E. Alvarez, N. Guillou, C. Martineau, B. Bueken, B. Van de Voorde, C. Le Guillouzer, P. Fabry, F. Nouar, F. Taulelle, D. De Vos, *Angew. Chem., Int. Ed.* **2015**, *54*, 3664.

[102] a) T. Ahnfeldt, D. Gunzelmann, J. Wack, J. Senker, N. Stock, *CrystEngComm* **2012**, *14*, 4126; b) A. Dhakshinamoorthy, N. Heidenreich, D. Lenzen, N. Stock, *CrystEngComm* **2017**, *19*, 4187.

[103] H. Reinsch, M. A. van der Veen, B. Gil, B. Marszalek, T. Verbiest, D. De Vos, N. Stock, *Chem. Mater.* **2013**, *25*, 17.

[104] a) P. Horcajada, T. Chalati, C. Serre, B. Gillet, C. Sebrie, T. Baati, J. F. Eubank, D. Heurtaux, P. Clayette, C. Kreuz, *Nat. Mater.* **2010**, *9*, 172; b) R. Singh, N. Gautam, A. Mishra, R. Gupta, *Indian J. Pharmacol.* **2011**, *43*, 246; c) P. B. Tchounwou, C. G. Yedjou, A. K. Patlolla, D. J. Sutton, in *Molecular, Cclinical and Environmental Toxicology*, Springer, Berlin, Germany **2012**, p. 133; d) B. Venugopal, T. D. Luckey, Metal Toxicity in Mammals. Vol. *2. Chemical Toxicity of Metals and Metalloids*, Plenum Press, New York, NY **1978**; e) J. Domingo, *J. Toxicol. Environ. Health, Part A* **1994**, *42*, 123.

[105] a) M. Taddei, *Coord. Chem. Rev.* **2017**, *343*, 1; b) H. Wu, Y. S. Chua, V. Krungleviciute, M. Tyagi, P. Chen, T. Yildirim, W. Zhou, *J. Am. Chem. Soc.* **2013**, *135*, 10525; c) O. V. Gutov, M. G. Hevia, E. C. Escudero-Adán, A. Shafir, *Inorg. Chem.* **2015**, *54*, 8396; d) P. Ghosh, Y. J. Colón, R. Q. Snurr, *Chem. Commun.* **2014**, *50*, 11329.

[106] a) M. Thommes, J. Morell, K. A. Cychosz, M. Fröba, *Langmuir* **2013**, *29*, 14893; b) M. Thommes, S. Mitchell, J. Pérez-Ramírez, *J. Phys. Chem. C* **2012**, *116*, 18816.